
ProtoVAE: A Trustworthy Self-Explainable Prototypical Variational Model

Srishti Gautam¹, Ahcene Boubekki¹, Stine Hansen¹, Suaiba Amina Salahuddin¹
Robert Jenssen¹, Marina MC Höhne^{2,1}, Michael Kampffmeyer¹

¹UiT The Arctic University of Norway

²Technical University of Berlin

Abstract

The need for interpretable models has fostered the development of self-explainable classifiers. Prior approaches are either based on multi-stage optimization schemes, impacting the predictive performance of the model, or produce explanations that are not transparent, trustworthy or do not capture the diversity of the data. To address these shortcomings, we propose ProtoVAE, a variational autoencoder-based framework that learns class-specific prototypes in an end-to-end manner and enforces *trustworthiness* and *diversity* by regularizing the representation space and introducing an orthonormality constraint. Finally, the model is designed to be *transparent* by directly incorporating the prototypes into the decision process. Extensive comparisons with previous self-explainable approaches demonstrate the superiority of ProtoVAE, highlighting its ability to generate trustworthy and diverse explanations, while not degrading predictive performance.

1 Introduction

Despite the substantial performance of deep learning models in solving various automated real-world problems, lack of transparency still remains a crucial point of concern. The black-box nature of these high-accuracy achieving models is a roadblock in critical domains such as healthcare [1, 2], law [3], or autonomous driving [4]. This has led to the emergence of the field of explainable artificial intelligence (XAI) which aims to justify or explain a model’s prediction in order to increase trustworthiness, fairness, and safeness in the application of the complex models henceforward.

Consequently, two lines of research have emerged within XAI. On the one hand, there are general methodologies explaining a posteriori black-box models, so-called post-hoc explanation methods [5, 6, 7]. While on the other hand, there are models developed to provide explanations along with their predictions [8, 9, 10]. The latter class of models, also known as self-explainable models (SEMs), are the focus of this work. Recently, many methods have been developed for quantifying post-hoc explanations [11]. However, there is still a lack of a concise definition of what SEMs should encompass, thus a lack of comparability of recent methods [12].

Methodologically, a large number of SEMs follow the approach of concept learning, analogous to prototype or basis feature learning, where a set of class representative features are learned [8, 9]. In this paper we gauge SEMs through the prism of three properties. First and foremost, the prototypes should be visualizable in the input space, and these transparent concepts should directly be employed by a glass-box classification model. Many of the existing approaches try to imitate prototype transparency by using nearest training samples to visualize the prototypes [8, 13], while some flatly use training images as prototypes preventing an end-to-end optimization and limiting the flexibility of the model [9, 14]. Secondly, the prototypes should exhibit both inter-class and intra-class diversity. Methods failing to ensure this property [9] are prone to prototype collapse into a single point which necessarily undermines their performance. Finally, SEMs should perform comparable to their black-

box counterparts while producing robust and faithful explanations. Previous approaches have a tendency to achieve self-explainability by sacrificing the predictive performance [9, 14, 13].

To address the aforementioned shortcomings of current SEMs, we introduce ProtoVAE, a prototypical self-explainable model based on a variational autoencoder (VAE) backbone. The architecture and the loss function are designed to produce *transparent*, *diverse*, and *trustworthy* predictions, as well as explanations, while relying on an end-to-end optimization. The predictions are linear combinations of distance-based similarity scores with respect to the prototypes in the feature space. The encoder and decoder are trained as a mixture of VAEs sharing the same network but each with its own Gaussian prior centered on one of the prototypes. The latter are enjoined to capture diverse characteristics of the data through a class-wise orthonormality constrain. Consequently, our learned prototypes are truly transparent global explanations that can be decoded and visualized in the input space. Further, we are able to generate local pixel-wise explanations by back-propagating relevances from the similarity scores. Empirically, our model corroborates trustworthiness both in terms of performance as well as the quality of its explanations.

Our main contributions can be summarized as follows:

- We define three properties for SEMs, based on which we present a novel prototypical self-explainable model with a variational auto-encoder backbone, equipped with a fully *transparent* prototypical space.
- We are able to learn faithful and *diverse* global explanations easily visualizable in the input space.
- We provide an extensive qualitative and quantitative analysis on five image classification datasets, demonstrating the efficiency and *trustworthiness* of our proposed method.

2 Predicates for a self-explainable model

For the benefit of an efficient and comprehensible formalization of SEMs, we here define three properties that we consider as prerequisites for SEMs.

Definition 1 An SEM is *transparent* if:

- (i) its concepts are utilized to perform the downstream task without leveraging a complex black-box model;
- (ii) its concepts are visualizable in input space.

Definition 2 An SEM is *diverse* if its concepts represent non-overlapping information in the latent space.

Definition 3 An SEM is *trustworthy* if:

- (i) the performance matches to that of the closest black-box counterpart;
- (ii) the explanations are robust, i.e., similar images yield similar explanations.
- (iii) the explanations represent the real contribution of the input features to the prediction.

Note that these definitions echo properties and axioms found in other works. However, the view of such properties is diverse across the literature which leads to failure of encompassing the wide research of SEMs in general. For example, *transparency* is known as ‘completeness’ in [15] and ‘local accuracy’ in [16]. In the next section, we provide a comparison of existing SEMs based on the fulfillment of the proposed predicates.

3 Categorization of related self-explainable works

Self-explainable models optimize for both explainability and prediction, making the network inherently interpretable. As our main contribution is a prototypical model, we review and categorize existing prototypical SEMs according to the above-mentioned properties.

SENN [8] introduces a general self-explainable neural network designed in stages to behave locally like a linear model. The model generates interpretable concepts, to which sample similarities are directly aggregated to produce predictions. This generalized approach has been followed by most of the prototypical and concept-based self-explainable methods, and is also mirrored by our approach. SENN, however uses training data to provide interpretation of learned concepts, therefore approximating transparency, unlike our model which by-design has a decoder to visualize prototypes.

Table 1: Summary of the SEM properties satisfied by the baselines. The optimization scheme is also indicated. The symbol \sim indicates that the concepts cannot be directly visualized in the input space and that the nearest training data serve as ersatz.

	Transparency	Diversity	Trustworthiness	Optimization
SENN[8]	\sim	✓	✓	End-to-end
ProtoPNet[9]	✓			Alternating
TesNET[14]	✓	✓		Alternating
SITE[17]		✓	✓	End-to-end
FLINT[13]	\sim	✓		End-to-end
ProtoVAE	✓	✓	✓	End-to-end

ProtoPNet [9] is a representative of a line of works [9, 14, 18, 19, 20], where a prototypical layer is introduced before the final classification layer. For maintaining interpretability, the prototypes are set as the projection of closest training image patches after every few iterations during training. Our method is closely related to ProtoPNet with the distinction of decode-able learned prototypes yielding a smooth and regularized prototypical space, thus allowing more flexibility in the model. TesNet [14] extends ProtoPNet and improves diversity at class level using five loss terms. Similarly to our approach, they distribute the base concepts among the classes and include an orthonormal constraint. However, the basis concepts are still projections from the nearest image patches, which leads to loss in predictive performance, similar to ProtoPNet. SITE [17] generates class prototypes from the input and introduces a transformation-equivariant model by constraining the interpretations before and after transformation. Since the prototypes are dynamic and generated for each test image, this method only provides local interpretations and lacks global interpretations. FLINT [13] introduces an interpreter model (FLINT- g) in addition to the original predictor model (FLINT- f). Although FLINT- f has been introduced by the authors as a framework that learns in parallel to the interpretations, it is not an SEM on its own. Therefore, we focus on FLINT- g , henceforward referred to as FLINT. FLINT takes as input features of several hidden layers of the predictor to learn a dictionary of attributes. However, the interpreter is not able to approximate the predictor model perfectly, therefore losing *trustworthiness*. Unlike prior approaches, ProtoVAE is designed to fulfill all three SEM properties. We summarize the discussed methods and their categorization in Table 1.

4 ProtoVAE

In this section, we introduce ProtoVAE, which is designed to obey the aforementioned SEM properties. Specifically, *transparency* is in-built in the architecture and further enforced along with *diversity* through the loss function. Also, we describe how our choices ensure the *trustworthiness* of our method.

4.1 Transparent architecture

In a *transparent* self-explainable model, the predictions are interpretable functions of concepts visualizable in the input space. To satisfy this property, we rely on an autoencoder-based architecture as backbone and a linear classifier. In order to have consistent, *robust*, and *diverse* global explanations, we consider prototypes in a greater number than classes. Unlike previous prototypical methods [9, 14], which update the prototypes every few iterations with the embeddings of the closest training images, ProtoVAE is trained *end-to-end* to learn both the prototypes in the feature space and the projection back to the input space. This gives ProtoVAE the flexibility to capture more general class characteristics. To further alleviate situations where some of the optimized prototypes are positioned far from the training data in the feature space, possibly causing poor reconstructions and interpretations, we leverage a variational autoencoder (VAE). VAEs are known to learn more robust embeddings and thus generate better reconstructions from out-of-distribution samples than simple autoencoders [21]. A schematic representation of the network is depicted in Fig. 1.

Details of the operations The downstream task at hand is the classification into $K > 0$ classes of the image dataset $\mathcal{X} = \{(\mathbf{x}_i, \mathbf{y}_i)\}_{i=1}^N$, where $\mathbf{x}_i \in \mathbb{R}^p$ is an image and the one-hot vector

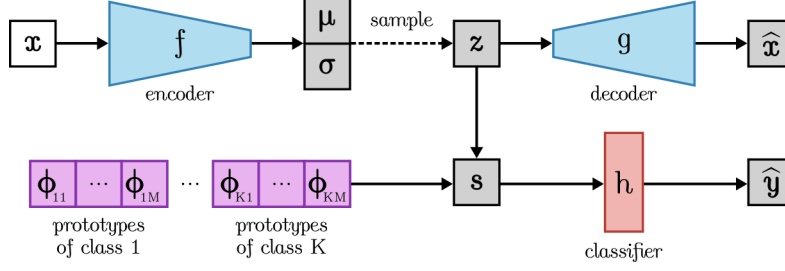


Figure 1: Schematic representation of the architecture of ProtoVAE. The input image x is encoded by f into a tuple (μ, σ) . A vector z is sampled from $\mathcal{N}(\mu, \sigma)$ which, on one side, is decoded by g into the reconstructed input \hat{x} and, on the other side, is compared to the prototypes $\phi_{k,j}$ resulting in the similarity scores s . The latter are passed through the classifier h to get the final prediction \hat{y} .

$y_i \in \{0, 1\}^K$ encodes its label. The network consists of an encoder $f : \mathbb{R}^p \rightarrow \mathbb{R}^d \times \mathbb{R}^d$, a decoder $g : \mathbb{R}^d \rightarrow \mathbb{R}^p$ ($d < p$), M prototypes per class $\Phi = \{\phi_{k,j}\}_{j=1..M}^{k=1..K}$, a similarity function $\text{sim} : \mathbb{R}^d \rightarrow \mathbb{R}^M$ and a glass-box linear classifier $h : \mathbb{R}^M \rightarrow [0, 1]^K$. An image x_i is first transformed by f into a tuple $(\mu_i, \sigma_i) = f(x_i)$ which, in the VAE realm, are the parameters of the posterior distribution. A feature vector z_i is then sampled from the normal distribution $\mathcal{N}(\mu_i, \sigma_i)$ and is used twice. On the one hand, it is decoded as $\hat{x}_i = g(z_i)$. On the other hand, it is compared to the prototypes. We use the same similarity function as in [9] and obtain the resulting vector $s_i \in \mathbb{R}^{K \times M}$ as:

$$s_i(k, j) = \text{sim}(z_i, \phi_{k,j}) = \log \left(\frac{\|z_i - \phi_{k,j}\|^2 + 1}{\|z_i - \phi_{k,j}\|^2 + \epsilon} \right), \quad (1)$$

with $0 < \epsilon < 1$. Finally, s_i is used to compute the predictions: $\hat{y}_i = h(s_i)$. Moreover, the similarity vector s_i captures the distance to the prototypes but also indicates the influence of each prototype on the prediction.

4.2 Diversity and trustworthiness

Unlike transparency, diversity cannot be achieved solely through the architectural choices. It needs to be further enforced during the optimization. Our architecture implies two loss terms: a classification loss and a VAE-loss. Without further regulation, our model is left vulnerable to the curse of prototype collapse [14, 22] which would undermine the SEM *diversity* property. We prevent such a situation with a third loss term enforcing orthonormality between prototypes of the same class. The loss function of ProtoVAE can thus be stated as follows:

$$\mathcal{L}_{\text{ProtoVAE}} = \mathcal{L}_{\text{pred}} + \mathcal{L}_{\text{orth}} + \mathcal{L}_{\text{VAE}}. \quad (2)$$

We detail now each term and discuss how they favor *diversity* and *trustworthiness*.

Inter-class diversity through classification Although the prototypes are assigned to a class, the classifier is blind to that information. Thus, the prediction problem is a classic classification that we solve using the cross-entropy loss.

$$\mathcal{L}_{\text{pred}} = \frac{1}{N} \sum_{i=1}^N \text{CE}(h(s_i); y_i). \quad (3)$$

Since h is linear, the loss pushes the embedding of each class to be linearly separable, yielding a greater *inter-class diversity* of the prototypes.

Intra-class diversity through orthonormalization The inter-class diversity is guaranteed by the previous terms. However, without further regularization, the prototypes might collapse to the center of the class, obviating the possibilities offered by the extra prototypes. To prevent such a situation and foster intra-class diversity, we enforce the prototype of each class to be orthonormal to each other as follows:

$$\mathcal{L}_{\text{orth}} = \sum_{k=1}^K \|\bar{\Phi}_k^T \bar{\Phi}_k - \mathbf{I}_M\|_F^2, \quad (4)$$

where \mathbf{I}_M is the identity matrix of dimension $M \times M$ and the column-vectors of matrix $\bar{\Phi}_k$ are the prototypes assigned to class k minus their mean, i.e., $\bar{\Phi}_k = \{\phi_{kj} - \bar{\phi}_k, j = 1 \dots M\}$ with $\bar{\phi}_k = \sum_{l=1}^M \phi_{kl}$. Beyond regularizing the Frobenius norm $\|\cdot\|_F$ of the prototype, this term favors the disentanglement of the captured concepts within each class, which is one way to obtain *intra-class diversity*.

Robust classification and reconstruction through VAE The VAE architecture ensures the robustness of the embedding and of the decoder. In its original form, the VAE loss considers a single standard normal distribution as a prior and is trained to minimize:

$$\|\mathbf{x} - \hat{\mathbf{x}}\|^2 + D_{\text{KL}}(p_f(z|\mathbf{x})||\mathcal{N}(\mathbf{0}_d, \mathbf{I}_d)), \quad (5)$$

where \mathbf{I}_d is the identity matrix of dimension $d \times d$. Such an objective enjoins the embedding to organize as if generated by a single Gaussian distribution, thus making it difficult to split it with the linear classifier h . To help the classifier, we consider instead a mixture of VAEs sharing the same network each with a Gaussian prior centered on one of the prototypes. Since, each prototype has a label, only data-points sharing that label are involved in the training of the associated VAE. The loss function of our mixture of VAEs is (derivation in the supplementary material Sec. S2):

$$\mathcal{L}_{\text{VAE}} = \frac{1}{N} \sum_{i=1}^N \|\mathbf{x}_i - \hat{\mathbf{x}}_i\|^2 + \sum_{k=1}^K \sum_{j=1}^M \mathbf{y}_i(k) \frac{\mathbf{s}_i(k, j)}{\sum_{l=1}^M \mathbf{s}_i(k, l)} D_{\text{KL}}(\mathcal{N}(\boldsymbol{\mu}_i, \boldsymbol{\sigma}_i) || \mathcal{N}(\phi_{kj}, \mathbf{I}_d)). \quad (6)$$

In addition to training the decoder, this loss enjoins the embedding to gather closely around their class prototypes.

4.3 Visualization of explanations

ProtoVAE is designed to have the inherent capability to reconstruct prototypes via the decoder, which is trained to approximate the input distribution. Additionally, to generate faithful pixel-wise local explanation maps, we build upon the concepts of Layer-wise relevance propagation (LRP) [23] which is a model-aware XAI method computing relevances based on the contribution of a neuron to the prediction. Following [12], we generate explanation maps, where for each prototype, the similarity of an input to the prototype is backpropagated to the input image according to the LRP rules. For an input image \mathbf{x}_i , the point-wise similarity between the transformed mean vector $\boldsymbol{\mu}_i$ with a prototype ϕ_{kj} is first calculated as:

$$\gamma_{ikj} = \frac{1}{\mathbf{d}_{ikj} + \eta} \quad \text{with} \quad \mathbf{d}_{ikj} = (\boldsymbol{\mu}_i - \phi_{kj}) * (\boldsymbol{\mu}_i - \phi_{kj}), \quad (7)$$

where $*$ is the Hadamard element-wise product and $\eta > 0$. The similarity γ_{ikj} is then backpropagated through the encoder following LRP composite rule, which is known as best practice [24] to compute local explanation maps. Following this, the $\text{LRP}_{\alpha\beta}$ rule is applied to the convolutional layers and the Deep Taylor Decomposition based rule DTD_{z^B} [25] is applied to the input features.

5 Experiments

In this section, we conduct extensive experiments to evaluate ProtoVAE’s trustworthiness, transparency, and ability to capture the diversity in the data. More specifically, we demonstrate the trustworthiness of our model in terms of predictive performance in Sec. 5.1. Qualitative evaluations are then conducted in Sec. 5.2 to verify the diversity and transparency properties, followed by a quantitative evaluation of the explanations corroborating its trustworthiness. Additionally, we provide an ablation study for the terms in Eq. 2 and further study the effect of the L2 norm in Eq. 6 on the prototype reconstructions in the supplementary material in Sec. S6.1 and Sec. S6.9, respectively.

Datasets and implementation: We evaluate ProtoVAE on 5 datasets, MNIST [26], FashionMNIST [27] (fMNIST), CIFAR-10, [28], a subset of QuickDraw [29] and SVHN [30]. We use small encoder networks with 4 convolution layers for MNIST, fMNIST and CIFAR-10, 3 for QuickDraw and 8 for SVHN. These convolution layers are followed by 2 linear layers which gives us the tuple $(\boldsymbol{\mu}_i, \boldsymbol{\sigma}_i)$ for each image i . The decoder mirrors the encoder’s architecture. Similar to [9], we fix

Table 2: Performance results of ProtoVAE compared to other state-of-the-art methods (measured in accuracy (in %)). The reported numbers are means and standard deviations over 4 runs. Best and statistically non-significantly different results are marked in bold. *Results for SITE are taken from the original paper and thus based on more complex architectures.

	Black-box encoder	FLINT [13]	SENN [8]	*SITE [17]	ProtoPNet [9]	ProtoVAE
MNIST	99.2±0.1	99.4±0.1	98.8±0.7	98.8	94.7±0.6	99.4±0.1
fMNIST	91.5±0.2	91.5±0.2	88.3±0.3	-	85.4±0.6	91.9±0.2
CIFAR-10	83.9±0.1	79.6±0.6	76.3±0.2	84.0	67.8±0.9	84.6±0.1
QuickDraw	86.7±0.4	82.6±1.4	79.3±0.3	-	58.7±0.0	87.5±0.1
SVHN	92.3±0.3	90.8±0.4	91.5±0.4	-	88.6±0.3	92.2±0.3

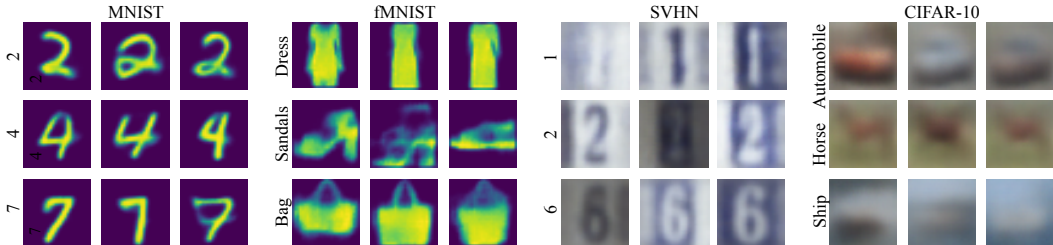


Figure 2: Visualization of learned prototypes for different classes for MNIST, fMNIST, SVHN and CIFAR-10.

the prototypes per class, M , to 5 for MNIST and SVHN and 10 for the other datasets. Further details about the datasets and additional implementation details, such as the detailed architecture and hyperparameters, are provided in the supplementary material Sec. S3 and S4. Our code is available at <https://github.com/SrishtiGautam/ProtoVAE>.

Baselines To ensure a fair comparison, we modified the publicly available code of ProtoPNet, FLINT and SENN to use the same backbone network as ProtoVAE and when relevant the same number of prototypes per class as used for ProtoVAE. We also provide the results for the predictive performance of SITE as reported in [17], since the code is not publicly available. We also report the performance of our model with a ResNet-18 backbone in the supplementary material Sec. S6.2. Further, we compare ProtoVAE using FLINT’s encoders as provided in [13] for both FLINT and SENN in Sec. S6.3 in the supplementary material. Finally, we also compare with the black-box counterpart of our model, i.e. a classical feed-forward CNN based on the same encoder as ProtoVAE but followed by a linear classifier and trained end-to-end with the cross-entropy loss. This black-box encoder model is thus free from all regularization necessary for self-explainability.

5.1 Evaluation of predictive performance

In the Table 2, we can observe that ProtoVAE surpasses all other SEMs in terms of predictive performance on all five datasets, which is based on its increased flexibility in the architecture. For ProtoPNet, we observe a gap in performance, which is due to the low number of optimal class-representatives in the actual training data. This creates a huge bottleneck at the prototype layer and therefore limits its performance. Further, and more importantly, when compared to the true black-box counterpart, ProtoVAE achieves no loss in accuracy and is even able to perform better on all the datasets. We believe this is due to an efficient over-clustering of the latent space with the flexible prototypes, as well as the natural regularizations achieved through the VAE model. These results strengthens the *trustworthiness* of ProtoVAE in terms of the predictive performance.

5.2 Evaluation of explanations

Qualitative evaluation The demonstrated results in this section strengthen the fulfilment of the *transparency* property by providing human-understandable explanations for ProtoVAE. We visualize the decoded prototypes for different datasets, which act as global explanations for the corresponding

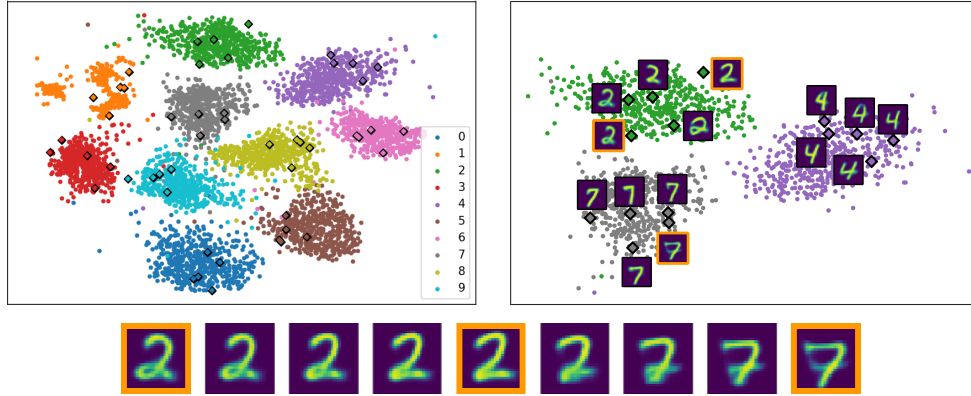


Figure 3: UMAP representations for the prototypical space for MNIST (left), decoded prototypes overlaid for classes 2, 4 and 7 (right), and interpolation between prototypes of the same class (2) and between prototypes of different classes (2-7) (bottom).

classes, in Fig. 2¹. The prototypes for MNIST demonstrate that class 2 consist of 2's with flat bottom line or with rounded bottom lines. For fMNIST, the sandals class consists of both heels and flats. The class prototypes thus directly help visualizing the components of the classes by looking at a fixed number of prototypes per class instead of all the training data. Interestingly, although SVHN often contains multiple digits of different classes in the same training image, our prototypes efficiently capture only one digit representing its class. Moreover, a blurring effect is observed in our prototypes which captures more variability and therefore suggests efficient representation of the true "mean" of a subset of a given class, as opposed to other methods [9, 14, 13] which show the closest training images and are therefore sharper. This behavior supports our claim of more flexibility in the network, therefore enhancing predictive capability along with the ability to provide more faithful explanations. This blurring effect is observed to be more prominent in CIFAR-10, which is due to the high complexity in each class in the dataset and can be reduced by using a larger number of prototypes per class.² Additionally, to provide more clear visualization of the learned transparent prototypical space, we show UMAP representations of the prototypes and the training data for MNIST in Fig. 3. This visualization further illustrates the inter-class as well as the intra-class *diversity* of the prototypes. Moreover, due to the regularized prototypical space, we are efficiently able to interpolate between prototypes both within a class and between classes, therefore making the latent space fully *transparent*. In Fig. 3, we interpolate between 2 different prototypes of class '2' and from a prototype of class '2' to a class '7' prototype.

The local explainability maps for a test image according to the three closest, i.e. most similar, prototypes for both ProtoVAE and ProtoPNet are shown in Fig. 4, along with the corresponding similarity scores. As seen, different prototypes of the same class activate different parts of the same test image, which therefore helps in achieving better performance. The ProtoPNet maps are extremely coarse which therefore makes them challenging to interpret. Therefore, we overlay the heatmaps over the input image for ProtoPNet. As observed, the most activated prototypes do not belong to the same class as the test image. This might happen because of ProtoPNet focusing on patches in prototypes, therefore losing contextual information. The 3 closest prototypes shown for the image 'apple' belong to class 'lion'. Further, an uninformative training image, which is not seen in the ProtoVAE prototypes, has been selected by ProtoPNet to represent 5 out of 10 prototypes for class 'lion'. The remaining 5 prototypes are represented by 1 other same training image. This effect is seen predominantly in ProtoPNet where the prototypes of the same class collapse to one point and are thus represented by the same training image, therefore dissatisfying the *diversity* property, as opposed to ProtoVAE. The prototypes for class 'lion' for both the models are included in the supplementary material in Sec. S6.4.

¹As a reference to gauge the quality and sharpness of the pictures of Fig. 2, reconstructions of test images are provided in Sec. S6.11.

²We demonstrate this behavior in Sec. S6.8 and show in Sec. S6.7 how local explainability maps can be used to gather additional information about pixel-wise relevances thereby counterbalancing blurry prototypes.

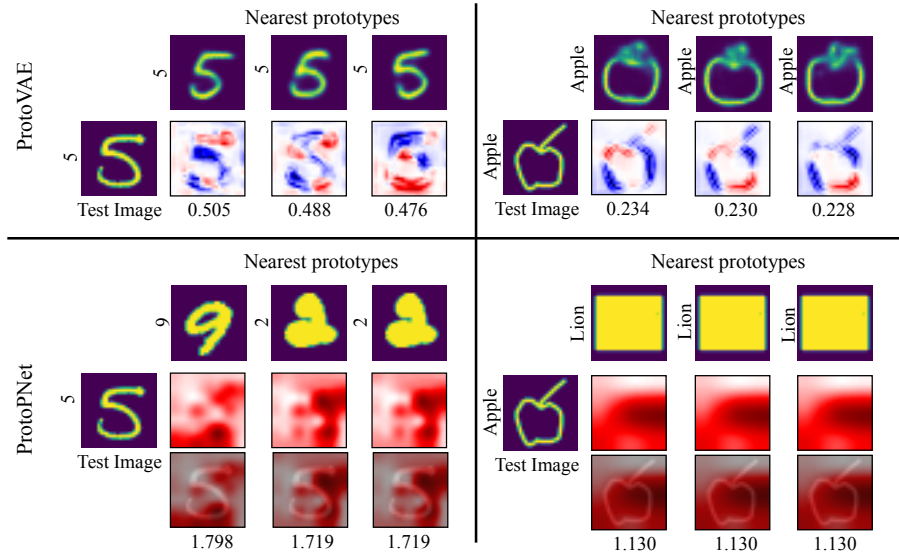


Figure 4: Three maximally activated prototypes, the corresponding prototypical activations, and corresponding similarity scores for a test image of class 5 (for MNIST) and apple (for QuickDraw), for both ProtoVAE and ProtoPNet models.

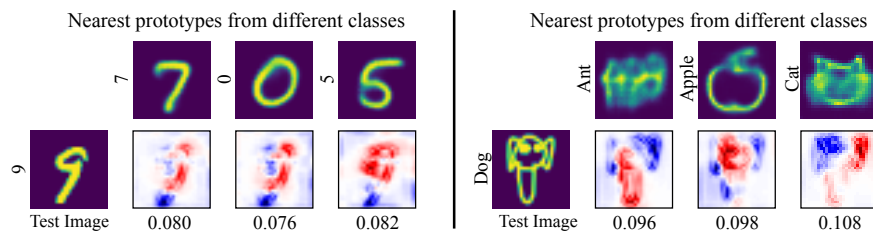


Figure 5: Maximally activated prototypes from three random classes, along with the prototypical explanations for MNIST (left) and QuickDraw (right) datasets.

We also show the closest prototypes from 3 different random classes and their corresponding explainability maps to demonstrate the behavior of explanations for different class prototypes in Fig. 5. Interestingly, the ‘dog’ image from the QuickDraw dataset resembles an ‘ant’ prototype for the legs, an ‘apple’ prototype for the face and a ‘cat’ prototype for the ears. This information provided by the local explainability maps thus aligns well with human-understandable concepts.

To compare the efficacy of the mapping to the input space learned by our decoder, to methodologies with training-data projection of prototypes [9, 14], we show prototypes along with the 3 closest training images for different datasets in Fig. 6. The prototypes are observed to be the representative of a subset of the respective class. For example, the prototype shown for class ‘4’ of MNIST is representing the subset of ‘4’ with an extended bar, while the ‘banana’ prototype represents the left facing ‘banana’ subset, and the ‘dog’ prototype represents the subset of white dogs on a darker background.

Finally, in order to demonstrate the scalability of ProtoVAE and its applicability on complex higher-resolution real world datasets, we provide an analysis on the CelebA dataset [31] in Sec. S6.10. Note that the less important and fairly diverse features (such as background) appear blurry, while the more important features (skin color, hair color, hair style or age) are crisp and clearly visible.

Quantitative evaluation To quantify the *trustworthiness* of the explanations provided by the proposed model, we calculate the Average Drop (AD) and Average Increase (AI) with respect to local explanation maps and similarity scores for all prototypes [32, 2]. The AD measures the decrease in similarity scores with respect to each prototype when the 50% least important pixels are removed from the images, while AI estimates the ratio of increasing similarity scores. A low AD and a high

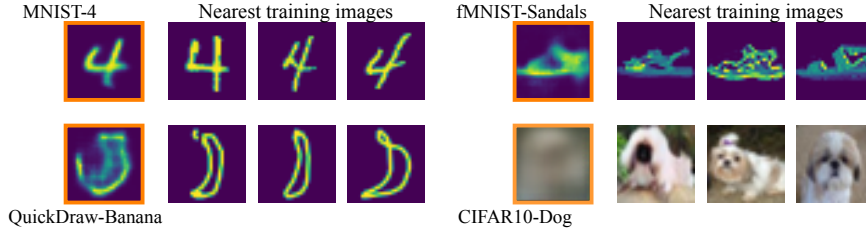


Figure 6: The three closest training images to the learned prototypes for MNIST (class ‘4’), QuickDraw (class ‘Banana’), fMNIST (class ‘Sandals’) and CIFAR-10 (class ‘Dog’), proving our prototypes representing a “real mean” of subset of classes.

Table 3: AD and AI for quantitative evaluation of explanations of ProtoVAE and ProtoPNet. The reported numbers are means and standard deviations over 5 runs. Best and statistically non-significantly different results are marked in bold.

	MNIST		fMNIST		CIFAR-10		QuickDraw		SVHN	
	AD	AI	AD	AI	AD	AI	AD	AI	AD	AI
ProtoPNet	3.4±0.3	0.6±0.0	7.2±0.4	0.5±0.0	11.6±0.2	0.5±0.0	2.6±0.1	0.7±0.0	5.4±0.0	0.7±0.0
ProtoVAE	0.4±0.0	0.6±0.0	5.1±0.0	0.8±0.0	6.6±0.0	0.7±0.0	0.1±0.0	0.9±0.0	6.1±0.1	0.7±0.0

AI suggest better performance. These scores are computed as follows:

$$AD = \frac{100}{NKM} \sum_{i=1}^N \sum_{k=1}^K \sum_{j=1}^M \frac{\max(0, \mathbf{s}_i(k, j) - \mathbf{s}_i^{50\%}(k, j))}{\mathbf{s}_i(k, j)}, \quad AI = \frac{\sum_{i=1}^N \sum_{k=1}^K \sum_{j=1}^M \mathbb{I}[\mathbf{s}_i(k, j) < \mathbf{s}_i^{50\%}(k, j)]}{NKM},$$

where $\mathbf{s}_i(k, j)$ is the similarity score of an image i with prototype j of class k (see Eq.1) and $\mathbf{s}_i^{50\%}(k, j)$ is the similarity score after masking the 50% least activated pixels according to the prototypical explanation map of prototype j . Also, $\mathbb{I}[\cdot]$ are the Iverson brackets which take the value 1 if the statement they contain is satisfied and 0 otherwise.

We report the mean and standard deviation for AD and AI computed over 5 random subsets of 1000 test images for ProtoVAE and ProtoPNet in Table 3. For the grayscale datasets, MNIST and fMNIST, the masked pixels are replaced by 0. For CIFAR-10 and SVHN, they are replaced by random uniformly sampled values. ProtoVAE achieves considerably lower AD and higher or comparable AI for all the datasets. For SVHN, ProtoPNet performs well which we believe is due to the abundance of representative patches in the dataset, thereby improving its explanations.

Finally, we perform a relevance ordering test [33, 12], where we start from a random image and monitor the predicted class probabilities while gradually adding a percentage of the most relevant pixels to the random image according to the local explanation maps. We take 100 random test images and report the average results of change in predicted class probability for all the prototypes in the model. The rate distortion graphs are shown in Fig. 7 for MNIST, QuickDraw and SVHN. We also include two baselines, Random-ProtoPNet and Random-ProtoVAE, where the pixel relevances are ordered randomly. Larger area under the curve indicates better performance. As shown, ProtoVAE’s local explanations are able to capture more relevant information than ProtoPNet for all three datasets. Further, for MNIST, ProtoPNet is performing even worse than Random-ProtoPNet, highlighting the lack of trustworthiness in ProtoPNet’s explanations.

6 Conclusion and Discussion

In this work, we define three properties that act as prerequisites for efficient development of SEMs, namely, *transparency*, *diversity*, and *trustworthiness*. We then introduce ProtoVAE, a prototypical self-explainable method, based on a variational auto-encoder backbone, which addresses these three properties. ProtoVAE incorporates a transparent model and enforces diversity and trustworthiness through the loss functions. In addition to providing faithful explanations, ProtoVAE is able to achieve better predictive performance than its counterpart black-box models.

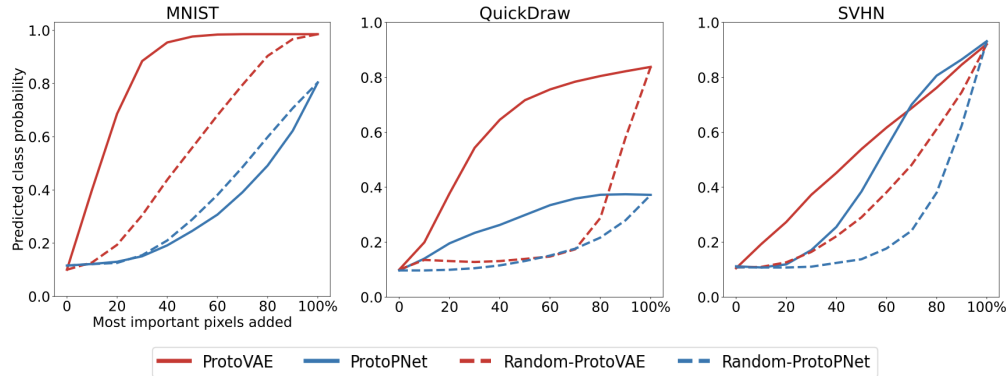


Figure 7: Relevance ordering test for ProtoPNet and ProtoVAE, along with the respective random baselines (Random-ProtoPNet and Random-ProtoVAE). Higher curve suggests better performance of ProtoVAE for all 3 datasets of MNIST, QuickDraw and SVHN.

The main limitation of ProtoVAE is the fixed number of prototypes. This means that the model has to grasp simple as well as more complex classes with the same number of prototypes. For example, in MNIST, there are more variations to be captured by the prototypes in the class ‘4’ than in class ‘1’. A simple but effective solution is a distance-based pruning procedure, which will be explored in future works. Another approach in sight is to use a prior on the distribution of the prototypical similarities and prioritize some prototypes by controlling the frequency with which each prototype is used in the predictions. Finally, since our global explanations can only be as good as the decoder, one more promising research direction is to leverage more expressive generative models, such as "Very Deep VAEs" [34] and normalizing flows [35] to further improve the scalability of the method to more complex datasets.

Acknowledgments and Disclosure of Funding

This work was financially supported by the Research Council of Norway (RCN), through its Centre for Research-based Innovation funding scheme (Visual Intelligence, grant no. 309439), and Consortium Partners. The work was further partially funded by RCN FRIPRO grant no. 315029 and RCN IKTPLUSS grant no. 303514. Moreover, the work was partly supported by the German Ministry for Education and Research through the third-party funding project Explaining 4.0 (ref. 01IS20055).

References

- [1] Alex J DeGrave, Joseph D Janizek, and Su-In Lee. AI for radiographic COVID-19 detection selects shortcuts over signal. *Nature Machine Intelligence*, 3(7):610–619, 2021.
- [2] Srishti Gautam, Marina M.-C. Höhne, Stine Hansen, Robert Jenssen, and Michael Kampffmeyer. Demonstrating the risk of imbalanced datasets in chest x-ray image-based diagnostics by prototypical relevance propagation. In *2022 IEEE 19th International Symposium on Biomedical Imaging (ISBI)*, pages 1–5, 2022.
- [3] Cynthia Rudin. Stop explaining black box machine learning models for high stakes decisions and use interpretable models instead. *Nature Machine Intelligence*, 1(5):206–215, 2019.
- [4] Daniel Omeiza, Helena Webb, Marina Jirotko, and Lars Kunze. Explanations in autonomous driving: A survey. *IEEE Transactions on Intelligent Transportation Systems*, pages 1–21, 2021.
- [5] Marco Tulio Ribeiro, Sameer Singh, and Carlos Guestrin. "why should i trust you?": Explaining the predictions of any classifier. *KDD '16*, page 1135–1144, 2016.
- [6] Ramprasaath R. Selvaraju, Michael Cogswell, Abhishek Das, Ramakrishna Vedantam, Devi Parikh, and Dhruv Batra. Grad-cam: Visual explanations from deep networks via gradient-based localization. In *2017 IEEE International Conference on Computer Vision (ICCV)*, pages 618–626, 2017.

- [7] Jason Yosinski, Jeff Clune, Anh M Nguyen, Thomas J. Fuchs, and Hod Lipson. Understanding neural networks through deep visualization. *ICML Deep Learning Workshop*, 2015.
- [8] David Alvarez Melis and Tommi Jaakkola. Towards robust interpretability with self-explaining neural networks. In S. Bengio, H. Wallach, H. Larochelle, K. Grauman, N. Cesa-Bianchi, and R. Garnett, editors, *Advances in Neural Information Processing Systems*, volume 31. Curran Associates, Inc., 2018.
- [9] Chaofan Chen, Oscar Li, Daniel Tao, Alina Barnett, Cynthia Rudin, and Jonathan K Su. This looks like that: Deep learning for interpretable image recognition. In H. Wallach, H. Larochelle, A. Beygelzimer, F. d'Alché-Buc, E. Fox, and R. Garnett, editors, *Advances in Neural Information Processing Systems*, volume 32. Curran Associates, Inc., 2019.
- [10] Sascha Saralajew, Lars Holdijk, Maike Rees, Ebubekir Asan, and Thomas Villmann. Classification-by-components: Probabilistic modeling of reasoning over a set of components. In *NeurIPS*, 2019.
- [11] Anna Hedström, Leander Weber, Dilyara Bareeva, Franz Motzkus, Wojciech Samek, Sebastian Lapuschkin, and Marina M.-C. Höhne. Quantus: An explainable ai toolkit for responsible evaluation of neural network explanations. 2022.
- [12] Srishti Gautam, Marina M. C. Höhne, Stine Hansen, Robert Jenssen, and Michael Kampffmeyer. This looks more like that: Enhancing self-explaining models by prototypical relevance propagation. *arXiv*, 2021.
- [13] Jayneel Parekh, Pavlo Mozharovskyi, and Florence d'Alché-Buc. A framework to learn with interpretation. In M. Ranzato, A. Beygelzimer, Y. Dauphin, P.S. Liang, and J. Wortman Vaughan, editors, *Advances in Neural Information Processing Systems*, volume 34, pages 24273–24285. Curran Associates, Inc., 2021.
- [14] Jiaqi Wang, Huafeng Liu, Xinyue Wang, and Liping Jing. Interpretable image recognition by constructing transparent embedding space. In *2021 IEEE/CVF International Conference on Computer Vision (ICCV)*, pages 875–884, 2021.
- [15] Mukund Sundararajan, Ankur Taly, and Qiqi Yan. Axiomatic attribution for deep networks. In *Proceedings of the 34th International Conference on Machine Learning - Volume 70, ICML'17*, page 3319–3328. JMLR.org, 2017.
- [16] Scott M. Lundberg and Su-In Lee. A unified approach to interpreting model predictions. In *Proceedings of the 31st International Conference on Neural Information Processing Systems, NIPS'17*, page 4768–4777, Red Hook, NY, USA, 2017. Curran Associates Inc.
- [17] Yipei Wang and Xiaoqian Wang. Self-interpretable model with transformation equivariant interpretation. In M. Ranzato, A. Beygelzimer, Y. Dauphin, P.S. Liang, and J. Wortman Vaughan, editors, *Advances in Neural Information Processing Systems*, volume 34, pages 2359–2372. Curran Associates, Inc., 2021.
- [18] Eunji Kim, Siwon Kim, Minji Seo, and Sungroh Yoon. Xprotonet: Diagnosis in chest radiography with global and local explanations. In *Proceedings of the IEEE/CVF Conference on Computer Vision and Pattern Recognition (CVPR)*, pages 15719–15728, June 2021.
- [19] Dawid Rymarczyk, Łukasz Struski, Jacek Tabor, and Bartosz Zieliński. Protopshare: Prototypical parts sharing for similarity discovery in interpretable image classification. In *Proceedings of the 27th ACM SIGKDD Conference on Knowledge Discovery & Data Mining, KDD '21*, page 1420–1430, New York, NY, USA, 2021. Association for Computing Machinery.
- [20] Meike Nauta, Ron van Bree, and Christin Seifert. Neural prototype trees for interpretable fine-grained image recognition. In *Proceedings of the IEEE/CVF Conference on Computer Vision and Pattern Recognition (CVPR)*, pages 14933–14943, June 2021.
- [21] Alexander Camuto, Matthew Willetts, Stephen Roberts, Chris Holmes, and Tom Rainforth. Towards a theoretical understanding of the robustness of variational autoencoders. In *International Conference on Artificial Intelligence and Statistics*, pages 3565–3573. PMLR, 2021.

- [22] Li Jing, Pascal Vincent, Yann LeCun, and Yuandong Tian. Understanding dimensional collapse in contrastive self-supervised learning. *arXiv preprint arXiv:2110.09348*, 2021.
- [23] Sebastian Bach, Alexander Binder, Grégoire Montavon, Frederick Klauschen, Klaus-Robert Müller, and Wojciech Samek. On pixel-wise explanations for non-linear classifier decisions by layer-wise relevance propagation. *PLOS ONE*, 10(7):1–46, 07 2015.
- [24] M. Kohlbrenner, A. Bauer, S. Nakajima, A. Binder, W. Samek, and S. Lapuschkin. Towards best practice in explaining neural network decisions with lrp. In *IJCNN*, pages 1–7, 2020.
- [25] Grégoire Montavon, Sebastian Lapuschkin, Alexander Binder, Wojciech Samek, and Klaus-Robert Müller. Explaining nonlinear classification decisions with deep taylor decomposition. *Pattern Recognition*, 65:211–222, 2017.
- [26] Y. Lecun, L. Bottou, Y. Bengio, and P. Haffner. Gradient-based learning applied to document recognition. *Proceedings of the IEEE*, 86(11):2278–2324, 1998.
- [27] Han Xiao, Kashif Rasul, and Roland Vollgraf. Fashion-mnist: a novel image dataset for benchmarking machine learning algorithms. *CoRR*, abs/1708.07747, 2017.
- [28] Alex Krizhevsky. Learning multiple layers of features from tiny images. 2009.
- [29] David Ha and Douglas Eck. A neural representation of sketch drawings. In *International Conference on Learning Representations*, 2018.
- [30] Yuval Netzer, Tao Wang, Adam Coates, Alessandro Bissacco, Bo Wu, and Andrew Y. Ng. Reading digits in natural images with unsupervised feature learning. In *NIPS Workshop on Deep Learning and Unsupervised Feature Learning 2011*, 2011.
- [31] Ziwei Liu, Ping Luo, Xiaogang Wang, and Xiaoou Tang. Deep learning face attributes in the wild. In *Proceedings of International Conference on Computer Vision (ICCV)*, December 2015.
- [32] Jeong Ryong Lee, Sewon Kim, Inyong Park, Taejoon Eo, and Dosik Hwang. Relevance-cam: Your model already knows where to look. In *Proceedings of the IEEE/CVF Conference on Computer Vision and Pattern Recognition (CVPR)*, pages 14944–14953, June 2021.
- [33] Jan MacDonald, Stephan Wäldchen, Sascha Hauch, and Gitta Kutyniok. A rate-distortion framework for explaining neural network decisions. *ArXiv*, abs/1905.11092, 2019.
- [34] Rewon Child. Very deep vaes generalize autoregressive models and can outperform them on images. *arXiv preprint arXiv:2011.10650*, 2020.
- [35] Danilo Rezende and Shakir Mohamed. Variational inference with normalizing flows. In *International conference on machine learning*, pages 1530–1538. PMLR, 2015.

ProtoVAE: A Trustworthy Self-Explainable Prototypical Variational Model (Supplementary Material)

Srishti Gautam¹, Ahcene Boubekki¹, Stine Hansen¹, Suaiba Amina Salahuddin¹
Robert Jenssen¹, Marina MC Höhne^{2,1}, Michael Kampffmeyer¹

¹UiT The Arctic University of Norway

²Technical University of Berlin

S1 Introduction

In this supplementary document we provide additional details for the proposed ProtoVAE. Specifically, we provide the derivation to illustrate that ProtoVAE learns a mixture of VAEs, followed by additional dataset, training and implementation details. We further provide additional results including ablation studies for the loss terms, predictive performance using ResNet-18 [1] as encoder, further comparisons with FLINT [2], and demonstrate ProtoVAE’s ability to capture the diversity of the data using additional qualitative results. Finally, we discuss the potential negative societal impacts of the proposed method.

S2 Mixture of VAE Derivation

In this section, we provide the derivations leading to Eq. 6 in the main paper. First, let’s recall, that training a VAE aims to maximize the evidence lower bound (ELBO), which, assuming the prior on \mathbf{z} is a standard Gaussian distribution, can be stated as follows:

$$\mathcal{L}_{\text{ELBO}} = \mathbb{E}_{p_f(\mathbf{z}|\mathbf{x})}(\log p_g(\mathbf{x}|\mathbf{z})) - D_{\text{KL}}(p_f(\mathbf{z}|\mathbf{x})||\mathcal{N}(\mathbf{0}_d, \mathbf{I}_d)), \quad (1)$$

where f and g designate the encoder and decoder, respectively, with $p_f(\mathbf{z}|\mathbf{x})$ being the approximate posterior distribution and $p_g(\mathbf{x}|\mathbf{z})$ the likelihood distribution. Assuming that $\mathbf{x}|\mathbf{z}$ follows a Gaussian distribution with covariance $\frac{1}{2}\mathbf{I}_p$, the first term of the $\mathcal{L}_{\text{ELBO}}$ simplifies as follows:

$$\mathbb{E}_{p_f(\mathbf{z}|\mathbf{x})}(\log p_g(\mathbf{x}|\mathbf{z})) = -\|\mathbf{x} - \bar{\mathbf{x}}\|^2 + \text{Constants}. \quad (2)$$

Our proposed ProtoVAE model learns a mixture of VAEs sharing the same network each having a Gaussian prior centered on one of the prototypes. More precisely, we consider K mixtures of VAEs each with M components, i.e., one mixture per class and one component per prototype. Each mixture is trained using the training data of one class $k \in 1, \dots, K$ and the mixture weights are given by the corresponding similarities of all M class prototypes, which are normalized as follows:

$$\tilde{\mathbf{s}}_i(k, j) = \frac{\mathbf{s}_i(k, j)}{\sum_{l=1}^M \mathbf{s}_i(k, l)}.$$

Hence, the loss function becomes:

$$\begin{aligned} \mathcal{L}_{\text{VAE}} &= \frac{1}{N} \sum_{i=1}^N \sum_{k=1}^K \sum_{j=1}^M -\mathbf{y}_i(k) \tilde{\mathbf{s}}_i(k, j) \mathcal{L}_{\text{ELBO}}(i, k, j). \\ &= \frac{1}{N} \sum_{i=1}^N \sum_{k=1}^K \sum_{j=1}^M \mathbf{y}_i(k) \tilde{\mathbf{s}}_i(k, j) \left(\|\mathbf{x}_i - \bar{\mathbf{x}}\|^2 - D_{\text{KL}}(\mathcal{N}(\boldsymbol{\mu}_i, \boldsymbol{\sigma}_i)||\mathcal{N}(\boldsymbol{\phi}_{kj}, \mathbf{I}_d)) \right). \end{aligned} \quad (3)$$

Since \mathbf{y}_i is a one-hot encoded vector, the reconstruction term simplifies to:

$$\sum_{i=1}^N \sum_{k=1}^K \sum_{j=1}^M \mathbf{y}_i(k) \tilde{\mathbf{s}}_i(k, j) \|\mathbf{x}_i - \bar{\mathbf{x}}_i\|^2 = \sum_{i=1}^N \|\mathbf{x}_i - \bar{\mathbf{x}}_i\|^2 \sum_{j=1}^M \tilde{\mathbf{s}}_i(\mathbf{y}_i(k), j) = \sum_{i=1}^N \|\mathbf{x}_i - \bar{\mathbf{x}}_i\|^2. \quad (4)$$

Now, injecting this simplification into Eq. 3 yields Eq. 6 of the main paper:

$$\mathcal{L}_{\text{VAE}} = \frac{1}{N} \sum_{i=1}^N \|\mathbf{x}_i - \bar{\mathbf{x}}_i\|^2 - \sum_{k=1}^K \sum_{j=1}^M \mathbf{y}_i(k) \tilde{\mathbf{s}}_i(k, j) D_{\text{KL}}(\mathcal{N}(\boldsymbol{\mu}_i, \boldsymbol{\sigma}_i) \|\mathcal{N}(\boldsymbol{\phi}_{kj}, \mathbf{I}_d)). \quad (5)$$

S3 Dataset details

The additional details, including the number of classes, number of training and testing samples, image sizes and license for the datasets are provided in Table 1. For MNIST, fMNIST, CIFAR-10, and SVHN, the default splits are used for training and testing. For QuickDraw, we use the subset created by [13]¹, which consists of 10000 random images per class from the following 10 classes: ‘Ant’, ‘Apple’, ‘Banana’, ‘Carrot’, ‘Cat’, ‘Cow’, ‘Dog’, ‘Frog’, ‘Grapes’, ‘Lion’. Of the 10000 images, 8000 are used for training and 2000 for testing. As pre-processing, all datasets were normalized to lie in the range [-1,1]. No data augmentation was performed for MNIST, fMNIST, QuickDraw and SVHN. For CIFAR-10, we first used zero-padding of size 2 and afterwards cropped images of size 32x32, which were then further used for training, following [2]. We further apply color jittering, where brightness, contrast, saturation, and hue of an image are changed randomly, as well as random horizontal flipping with a probability of 0.5.

Table 1: Additional details for the open-source datasets used in this work.

	MNIST	Fashion-MNIST (fMNIST)	QuickDraw (subset [13])	CIFAR-10	SVHN
<i>No. of classes</i>	10	10	10	10	10
<i>Number of samples (Training)</i>	60,000	60,000	80,000	60,000	73,257
<i>Number of samples (Testing)</i>	10,000	10,000	20,000	10,000	26,032
<i>Image size</i>	28x28	28x28	28x28	32x32	32x32
<i>License</i>	CC BY-SA 3.0	MIT	CC BY 4.0	MIT	CC0 1.0

S4 Training and Implementation

All the experiments are conducted using PyTorch [3] with a NVIDIA GeForce GTX 1080 Ti GPU. The detailed network architectures for all datasets are shown in Figure 1. The hyperparameter settings used for different datasets are described in Table 2 for ProtoVAE, for the Black-box encoder in Table 3, and for ProtoPNet in Table 4. For ProtoPNet, the optimal values for learning rates and coefficients for the loss terms are used, as reported in [4].

Table 2: Hyperparameter and training settings for the different datasets for ProtoVAE.

	MNIST	fMNIST	CIFAR-10	QuickDraw	SVHN
<i>No. of prototypes per class</i>	5	10	10	10	5
<i>Size of feature vector (z)</i>	256	256	512	512	512
<i>No. of epochs</i>	10	10	36	10	10
<i>Batch size</i>	128	128	128	128	64
<i>Learning rate</i>	0.001	0.001	0.001	0.001	0.001

S5 Source Code

Our source code is available at <https://github.com/SrishtiGautam/ProtoVAE>.

¹<https://github.com/jayneelparekh/FLINT>

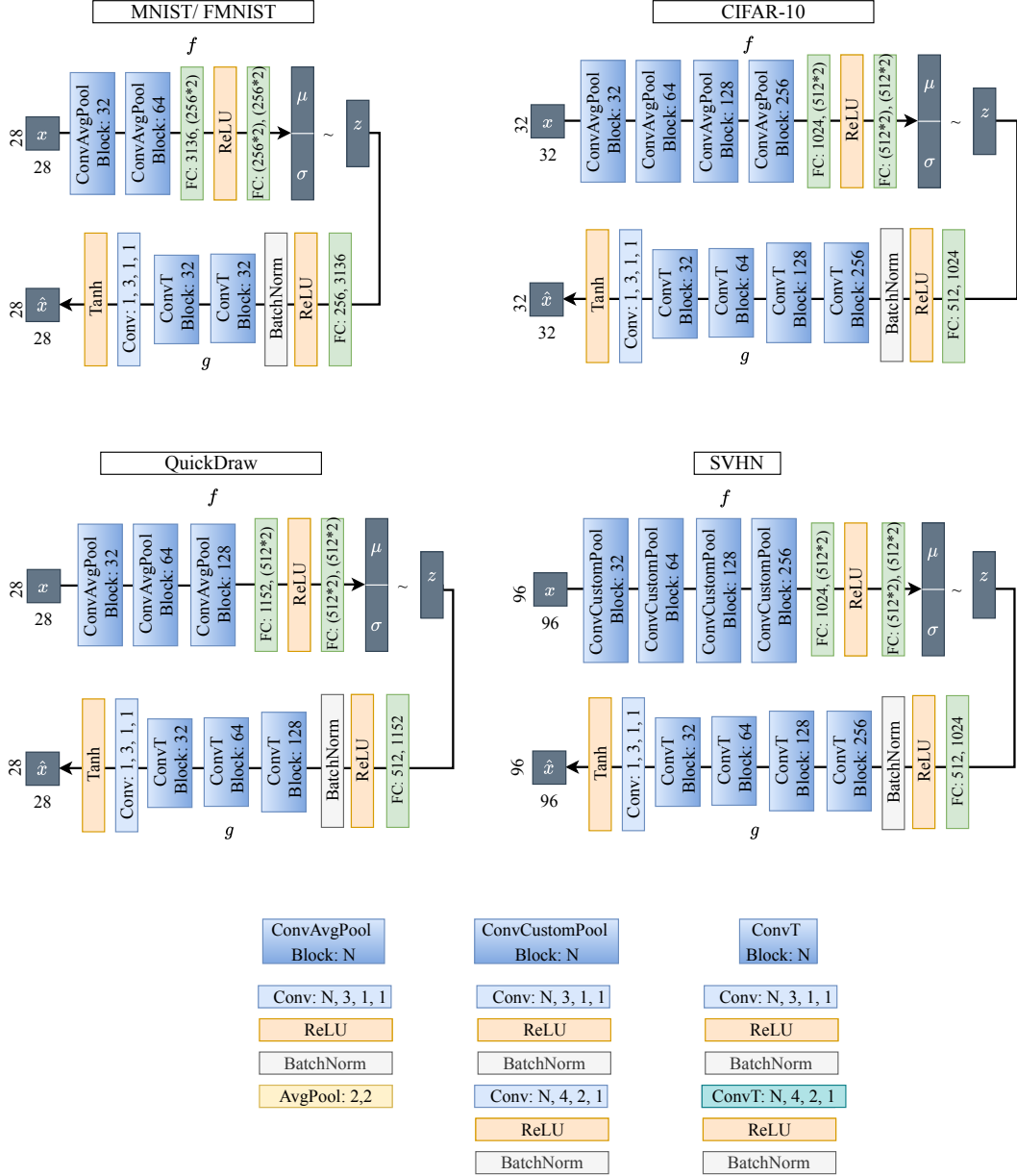


Figure 1: Visualization of the architectures used for the different datasets. f is the encoder and g the decoder. Conv: i,j,k,l represents the convolutional layer with number of output channels i , kernel size j , stride k and padding l . FC: i,j represents the fully connected layer with i input neurons and j output neurons. ConvT represents a transposed convolutional layer. AvgPool: i,j represents average pooling layer with kernel size i and stride j .

Table 3: Hyperparameter and training settings for the different datasets for Black-box encoder.

	MNIST	fMNIST	CIFAR-10	QuickDraw	SVHN
<i>No. of epochs</i>	10	10	40	4	7
<i>Batch size</i>	128	128	128	128	64
<i>Learning rate</i>	0.001	0.001	0.001	0.001	0.001

Table 4: Hyperparameter and training settings for the different datasets for ProtoPNet.

	MNIST	fMNIST	CIFAR-10	QuickDraw	SVHN
<i>Prototype shape</i>	(50,256,1,1)	(100,256,1,1)	(100,512,1,1)	(100,512,1,1)	(50,512,1,1)
<i>No. of epochs</i>	31	31	21	51	51
<i>Batch size</i>	128	128	128	128	64

S6 Additional Results

In this section, we provide additional quantitative as well as qualitative results for ProtoVAE.

S6.1 Ablation Study

In the following, we conduct an ablation study for the terms in Eq. 2 in the main paper. Specifically, we study the influence of the orthonormalization, ($\mathcal{L}_{\text{orth}}$) and the KL divergences (\mathcal{L}_{KL}), where:

$$\mathcal{L}_{\text{orth}} = \sum_{k=1}^K \|\bar{\Phi}_k^T \bar{\Phi}_k - \mathbf{I}_M\|_F^2, \tag{6}$$

$$\mathcal{L}_{\text{KL}} = \sum_{k=1}^K \sum_{j=1}^M \mathbf{y}_i(k) \frac{\mathbf{s}_i(k, j)}{\sum_{l=1}^M \mathbf{s}_i(k, l)} D_{\text{KL}}(\mathcal{N}(\boldsymbol{\mu}_i, \boldsymbol{\sigma}_i) \parallel \mathcal{N}(\boldsymbol{\phi}_{kj}, \mathbf{I}_d)) \tag{7}$$

\mathcal{L}_{KL} is the second term in the \mathcal{L}_{VAE} loss (see Eq. 6 in the main paper). The predictive performance for the MNIST dataset in the presence of: (i) the full loss ($\mathcal{L}_{\text{ProtoVAE}}$), i.e, with the presence of both the above mentioned terms, (ii) without $\mathcal{L}_{\text{orth}}$, i.e, $\mathcal{L}_{\text{ProtoVAE}} - \mathcal{L}_{\text{orth}}$, (iii) without \mathcal{L}_{KL} , i.e, $\mathcal{L}_{\text{ProtoVAE}} - \mathcal{L}_{\text{KL}}$, and (iv) without both, i.e, $\mathcal{L}_{\text{ProtoVAE}} - \mathcal{L}_{\text{orth}} - \mathcal{L}_{\text{KL}}$ is provided in Table 5. Further, the prototypes learned in the presence of full loss and in the absence of $\mathcal{L}_{\text{orth}}$ and \mathcal{L}_{KL} are shown in Fig. 2. The absence of the orthogonality term leads to a decrease in accuracy due to a collapse of prototypes to the center of the class. The absence of the KL term leads to a considerable drop in accuracy, as well as poor reconstructions of the prototypes.

Table 5: Ablation study: Prediction accuracy (in %) for MNIST dataset. Mean and standard deviation of 4 runs are provided.

	$\mathcal{L}_{\text{ProtoVAE}}$	without $\mathcal{L}_{\text{orth}}$	without \mathcal{L}_{KL}	without both
MNIST	99.4±0.1	99.2±0.1	58.8±10.7	98.9±0.1

S6.2 ProtoVAE with ResNet-18 encoder

In this section we provide the results for all 5 datasets using an ImageNet [5] pretrained ResNet-18 [1] as encoder f . The ResNet-18 layers are followed by add-on layers (the fully connected layers from the encoders in Fig. 1) to provide the same dimensional embeddings as the prior architectures. The decoders follow the same architecture as described in Fig. 1. The hyperparameter and training settings are further provided in Table 6. The predictive performance for all the datasets, as shown in Table 7 demonstrates the effectiveness of ProtoVAE even with a more complex architecture of ResNet-18, thus confirming its wide applicability.

Additionally, note that ProtoVAE can easily be modified for domains where a larger effect on different terms is desired. For example, if more clear global explanations are required for safety critical applications, such as healthcare, the reconstruction loss term can be assigned a higher weight. An example of prototypes learned for the SVHN dataset with ResNet-18 as encoder and 10 as the weight for the reconstruction term are shown in Fig. 3.

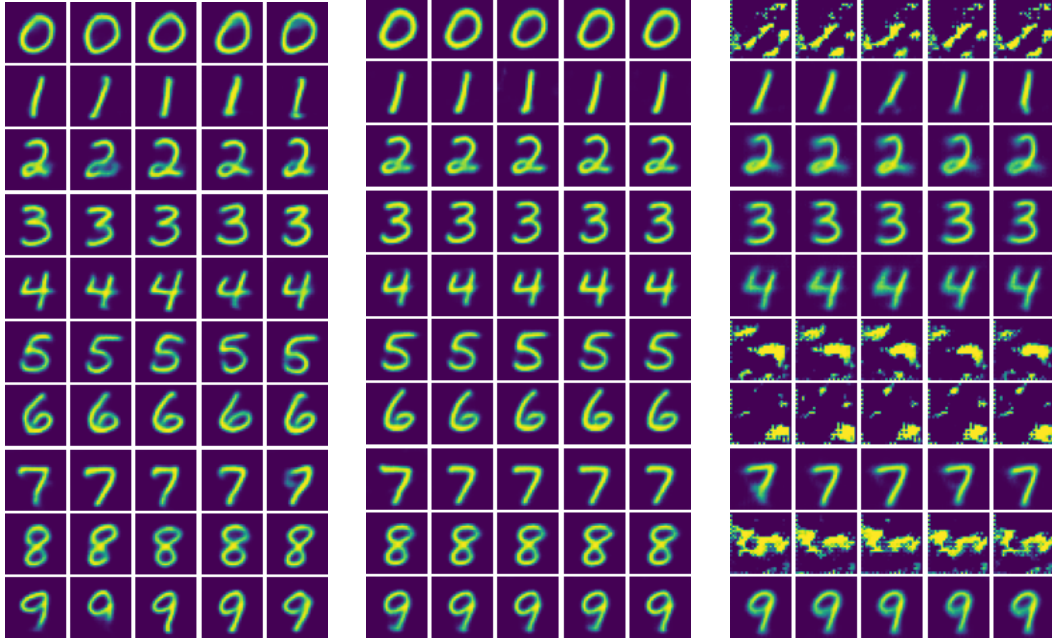


Figure 2: MNIST prototypes with full $\mathcal{L}_{\text{ProtoVAE}}$ loss (left), without $\mathcal{L}_{\text{orth}}$ (middle) and without \mathcal{L}_{KL} (right). The absence of $\mathcal{L}_{\text{orth}}$ leads to a collapse of prototypes to the center of the class. The absence of \mathcal{L}_{KL} leads to unreliable reconstructions due to the non-regularized prototype space.

Table 6: Hyperparameter and training settings for the different datasets for ProtoVAE with ResNet-18 as backbone.

	MNIST	fMNIST	CIFAR-10	QuickDraw	SVHN
<i>No. of prototypes per class</i>	5	10	10	10	5
<i>Size of feature vector (z)</i>	256	256	512	512	512
<i>No. of epochs</i>	15	15	36	15	15
<i>Batch size</i>	128	128	128	128	64
<i>Learning rate</i>	0.001	0.001	0.001	0.001	0.001

Table 7: Accuracy (in%) for ProtoVAE with ResNet-18 as backbone. The numbers provided are the mean and standard deviation of 4 runs.

	MNIST	fMNIST	CIFAR-10	QuickDraw	SVHN
<i>ProtoVAE (ResNet-18)</i>	99.4±0.0	91.9±0.1	80.5±0.4	86.3±0.3	92.2±0.2

S6.3 Comparison with FLINT

We compare the predictive performance of ProtoVAE to the one that FLINT (FLINT- g) and SENN obtain using FLINT’s more complex encoders as reported in [2] in Table 8. Even when using FLINT’s ResNet-18 [1] based architectures as backbones for QuickDraw and CIFAR-10, ProtoVAE still surpasses their accuracy while only using small encoders.

S6.4 ProtoPNet vs ProtoVAE: Diversity of prototypes

To demonstrate the importance of intra-class *diversity*, in this section we show a few prototypes for the QuickDraw dataset learned by ProtoPNet and ProtoVAE for class ‘Lion’ (Fig. 4), class ‘Banana’ (Fig. 5) and class ‘Carrot’ (Fig. 6). It is observed that ProtoPNet uses ‘artifact’ training images as prototypes very frequently for several classes, therefore failing to achieve competitive accuracy for



Figure 3: Prototypes learned for SVHN for ResNet-18 as encoder with weight for reconstruction loss as 10. The accuracy achieved by this model is 91.2%.

Table 8: Accuracy comparison (in %) with FLINT and SENN, where their results are obtained from [13]. Note that in this case FLINT and SENN uses more complex encoders, while ProtoVAE results are obtained only using the small encoder. The numbers provided are the mean and standard deviation of 4 runs.

	MNIST	fMNIST	CIFAR-10	QuickDraw
<i>ProtoVAE</i>	99.4±0.1	91.9±0.2	84.6±0.1	87.5±0.1
<i>FLINT</i> [2]	98.3±0.2	86.8±0.4	84.0±0.4	85.4±0.1
<i>SENN</i> [6]	98.4±0.1	84.2±0.3	77.8±0.7	85.5±0.4

this dataset. ProtoVAE on the other hand learns diverse prototypes, which are closer to the ‘true’ mean of the subset of classes, therefore acting as improved class representatives.

S6.5 ProtoPNet vs ProtoVAE: Patch and Image-based explanations

ProtoPNet provides patch-based explanations, where a patch from the training image is used by the network for classification. While, on the other hand, ProtoVAE uses full images as prototypes, which are used for classification. We provide a comparison of patch-based vs image-based explanations provided by these methods in Fig. 7 and observe that ProtoPNet loses contextual information due to their patch-based prototypes. This highlights their dependency on the original images where the prototype patches come from to be interpretable. ProtoVAE instead uses full image embeddings as

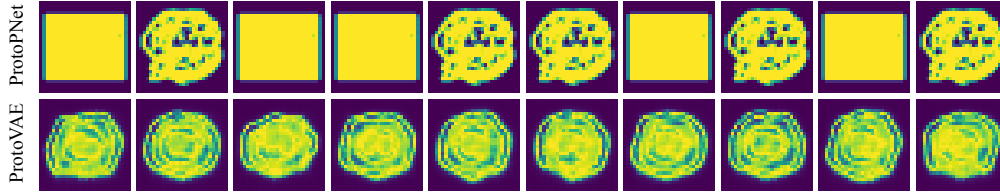


Figure 4: Prototypes learned by ‘Lion’ class of QuickDraw dataset for ProtoPNet (top) and ProtoVAE (bottom).

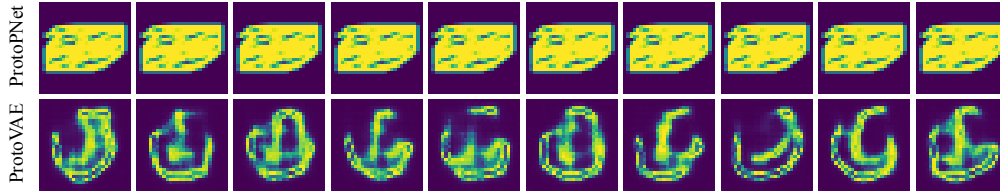


Figure 5: Prototypes learned by ‘Banana’ class of QuickDraw dataset for ProtoPNet (top) and ProtoVAE (bottom).

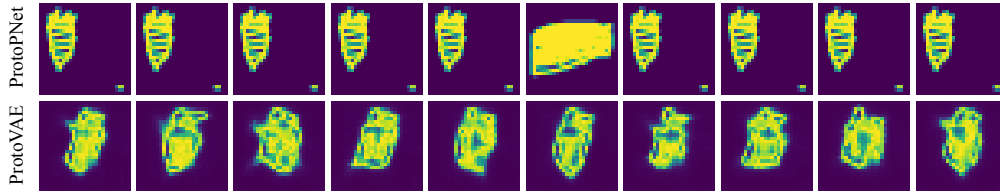


Figure 6: Prototypes learned by ‘Carrot’ class of QuickDraw dataset for ProtoPNet (top) and ProtoVAE (bottom).

prototypes, which efficiently represent the ‘true’ mean of class subsets and are thus fully interpretable on their own.

S6.6 ProtoPNet vs ProtoVAE: Visualization of prototypes

We compare the prototype visualization techniques used by ProtoPNet and ProtoVAE. While ProtoPNet imitates transparency by projecting prototypes to the closest training images, ProtoVAE has the capability to visualize the learned prototypes with the help of the in-built decoder architecture. We show the prototypes learned by ProtoPNet and ProtoVAE for the SVHN dataset in Fig 8. SVHN consists of many training samples with multiple digits in each image. Since ProtoPNet limits the prototypes to be represented by training samples, its prototypes images also capture images with multiple digits. ProtoVAE however allows more flexibility and interestingly learns prototypes that only capture the correct class digit.

S6.7 Enhanced interpretability by local explainability maps

While the quality of reconstruction is limited by the simple VAE, the robust local explainability maps produced by ProtoVAE offer an additional way to explain the predictions or the similarity scores in a situation where the visualizations of the prototypes are not very informative. In Figure 9, we show prototypical explanations generated using LRP for 4 test images from CIFAR-10 dataset. For each test image, the LRP maps for 2 prototypes from different classes are shown to analyse the area of interest in the test image by different class prototypes. As can be observed, the first test image

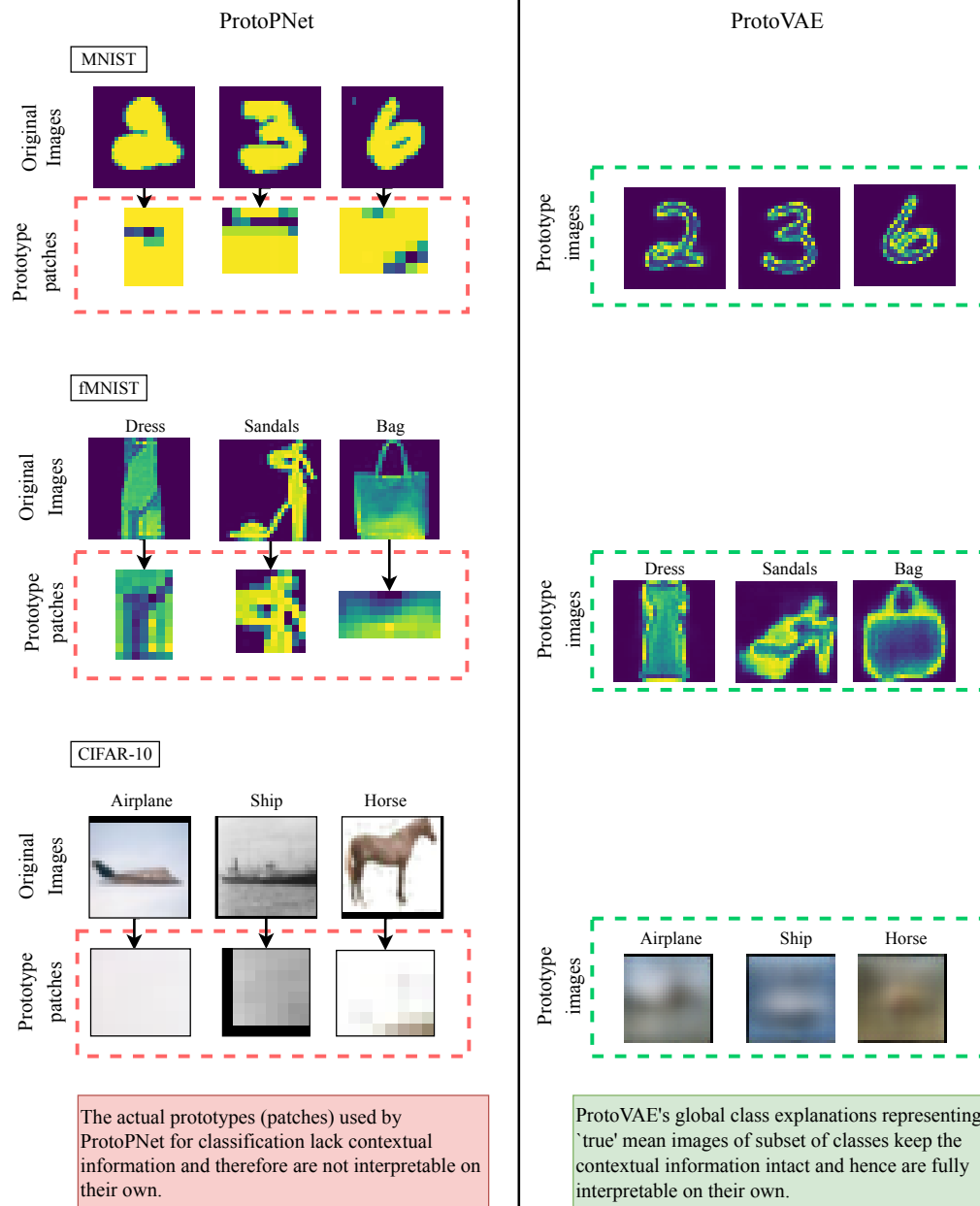


Figure 7: ProtoPNet vs ProtoVAE: Patch vs Image based global explanations.

(top left) has the positive relevance at the bottom of the aircraft for the horse prototype and positive relevance at the wheels and wheel-like objects as well as the sky for the automobile class prototype. The second test image (top right) has the head of the airplane resembling as an airplane and the shape near the wheels interestingly resembling a horse. The bottom left test image associates the shape of the ship with an airplane and a spherical shape resembling the wheel of an automobile. Finally, the bottom right test image has the front part of the vehicle activated by the automobile prototype and the top curved area resembling a ship.

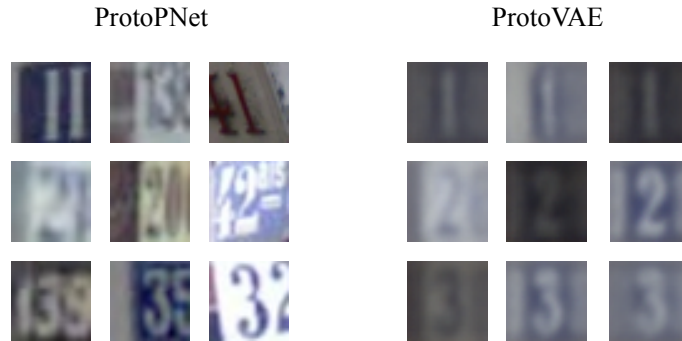


Figure 8: We show three learned prototypes for SVHN for ProtoPNet(left) and ProtoVAE(right). While the training data of SVHN consists of multiple digits in each image, ProtoPNet’s prototypes visualizations also capture multiple digit images. However, due to the flexibility of our model, it has been observed that ProtoVAE always captures one digit, i.e., representing more faithful class prototypes.

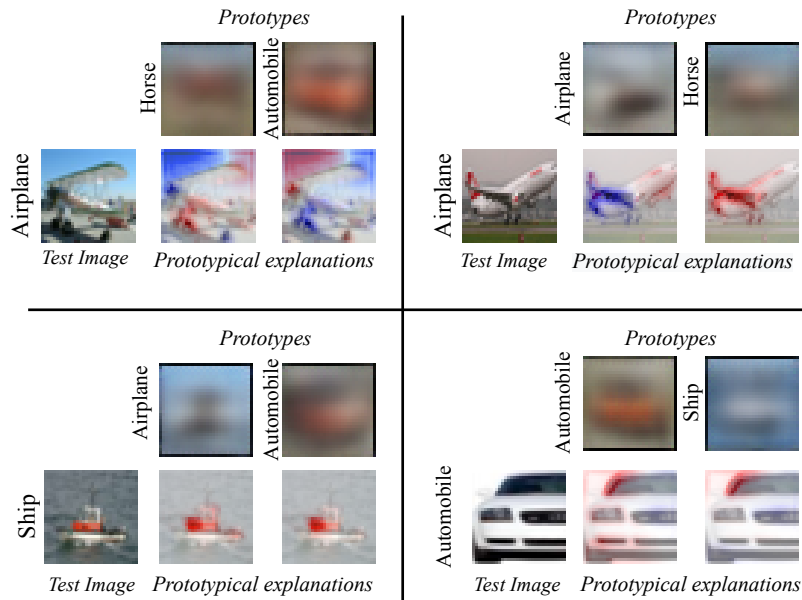


Figure 9: Prototypical explanations using LRP for CIFAR-10 dataset. For each test image, the prototypical explanations for 2 prototypes from different classes are provided.

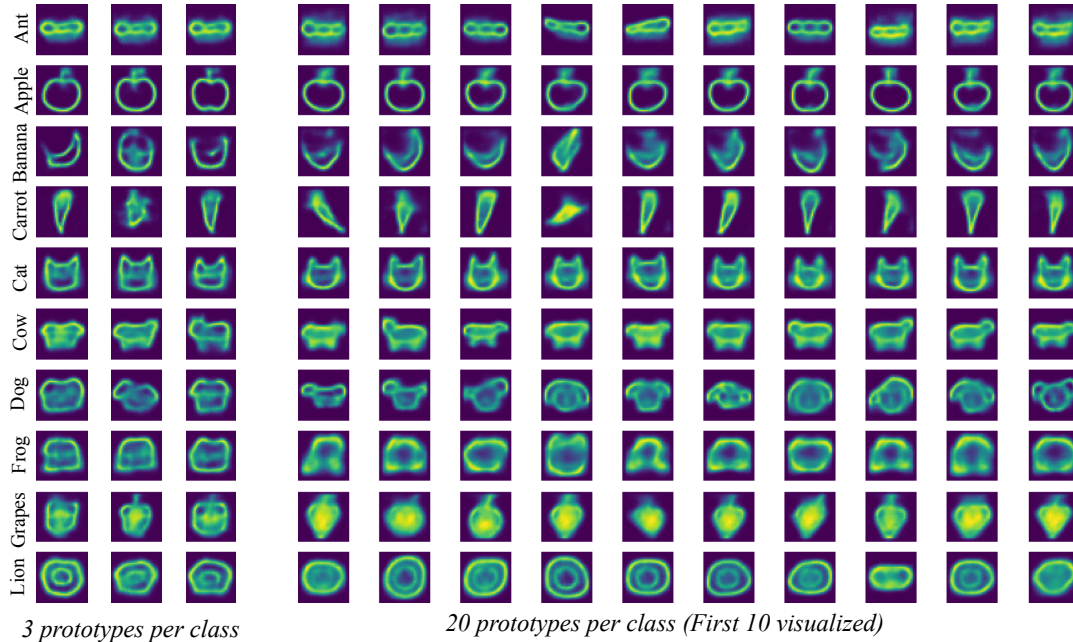


Figure 10: Effect on the sharpness of prototype reconstructions for QuickDraw when the number of prototypes per class are increased from 3 (top) to 20 (bottom). Sharpness can be observed for several classes (see Cat, Cow, Dog, Frog and Grapes, for example).

S6.8 Increasing number of prototypes per class

In this section, we demonstrate experimentally that the prototype reconstructions can get sharper as the number of prototypes per class increases. We show the results on QuickDraw (Figure 11) and CIFAR-10 (Figure 10 datasets). For QuickDraw, we show the difference between prototype reconstructions for ProtoVAE trained with 3 prototypes per class (Figure 11 left) and 20 prototypes per class (Figure 11 right). For CIFAR-10, we show the difference for models trained with 3, 5 and 20 prototypes per class (Figure 11). For both of the datasets the first 10 prototypes are visualized for the 20 prototypes per class trained models.

As observed for QuickDraw, we can see sharpness and added information in most of the classes. The largest effect of increased sharpness can be seen in classes Cat, Dog, Frog and Grapes. It can also be observed that the Dog prototypes are able to capture more variations of dogs, especially front view and side view as the number of prototypes increases. Similarly for CIFAR-10 we can see more variations of subsets of classes captured by prototypes when the number of prototypes increase thereby leading to less blurry prototype reconstructions. With only 3 prototypes per class, prototypes are degenerate and it is hard to guess that automobile prototypes depict cars. However, with 20 prototypes, we can see more orientations of cars captured by the model. The sharpness and variations captured by the prototypes can also be observed for other classes such as Dog, Horse etc.

S6.9 Effect of L2 norm on prototype reconstructions

To analyse the effect of the L2 norm, we demonstrate the prototypes learned with varying weight for the reconstruction loss term. The prototype reconstructions for QuickDraw for reconstruction loss weight 0.1 and 1 are shown in Figure 12 top and bottom, respectively and for 10 and 100 are shown in Figure 13 top and bottom, respectively. As can be clearly observed, the prototype reconstructions tend to be sharper with higher weight. This effect can be observed in all classes. For example, for the class Cat we start to see clear boundaries as well as whiskers when the weight is 100. We can further observe sharper grapes, dogs as well as frogs when we move from weight 0.1 to 100. Similarly, for CIFAR-10, we can observe more details present in the prototype reconstructions as the weight for the reconstruction loss is increased from 0.1 to 10 (see Figure 14). We can observe different colors and

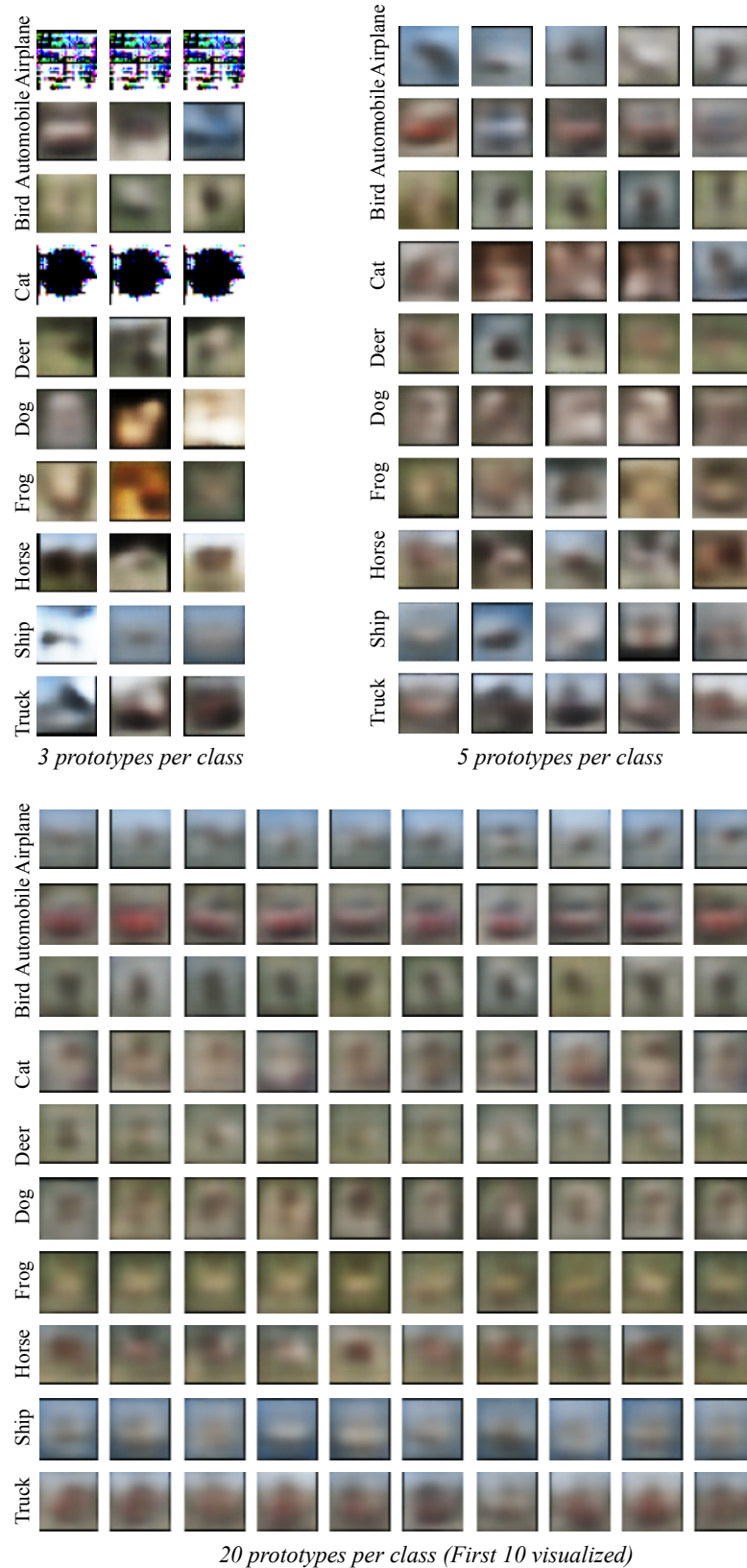
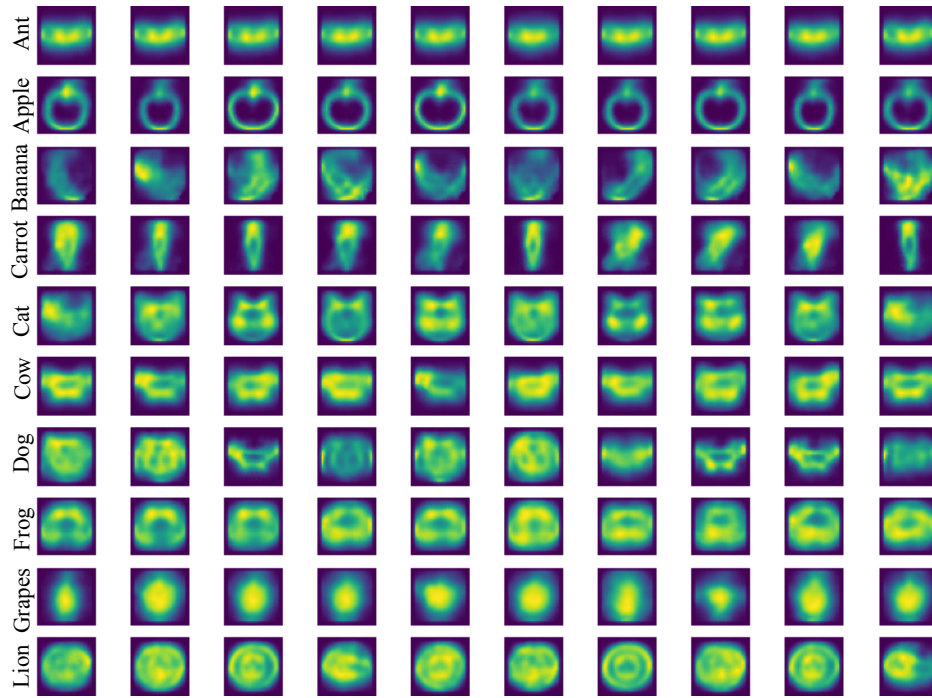
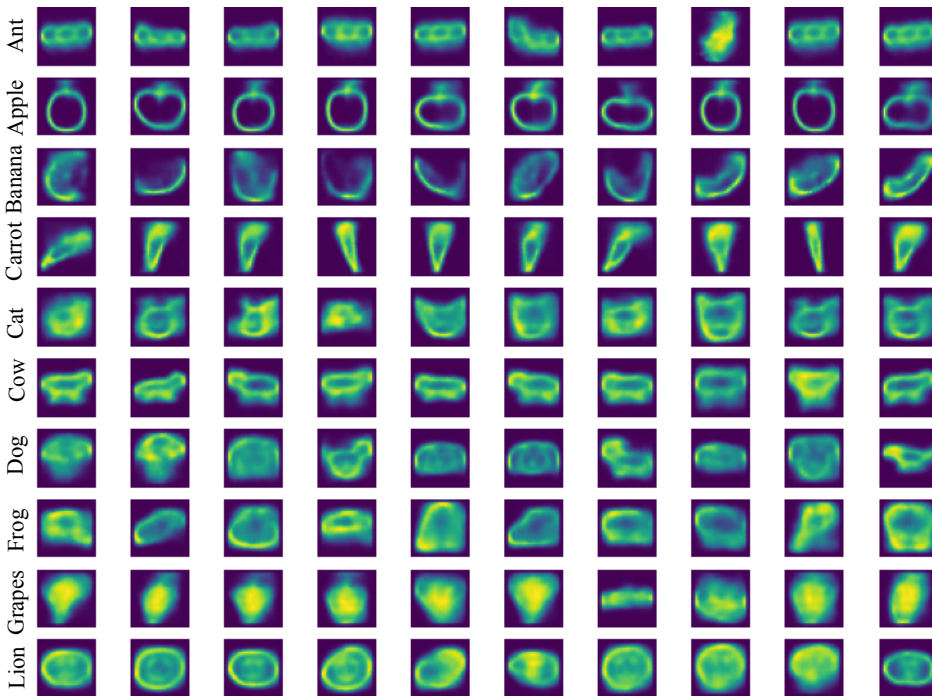


Figure 11: Effect on the sharpness of prototype reconstructions for CIFAR-10 for the models trained with 3, 5 and 20 number of prototypes per class. Less blurriness and more variations captured can be observed for several classes (see Automobile, Horse, Ship, for example).

orientations of automobiles captured as well as comparatively more detailed airplanes, horses and trucks for higher weight of the L2 norm.



Reconstruction loss weight=0.1



Reconstruction loss weight=1

Figure 12: Prototypes for models trained on QuickDraw dataset with reconstruction loss term weighted 0.1 (top) and 1 (bottom).

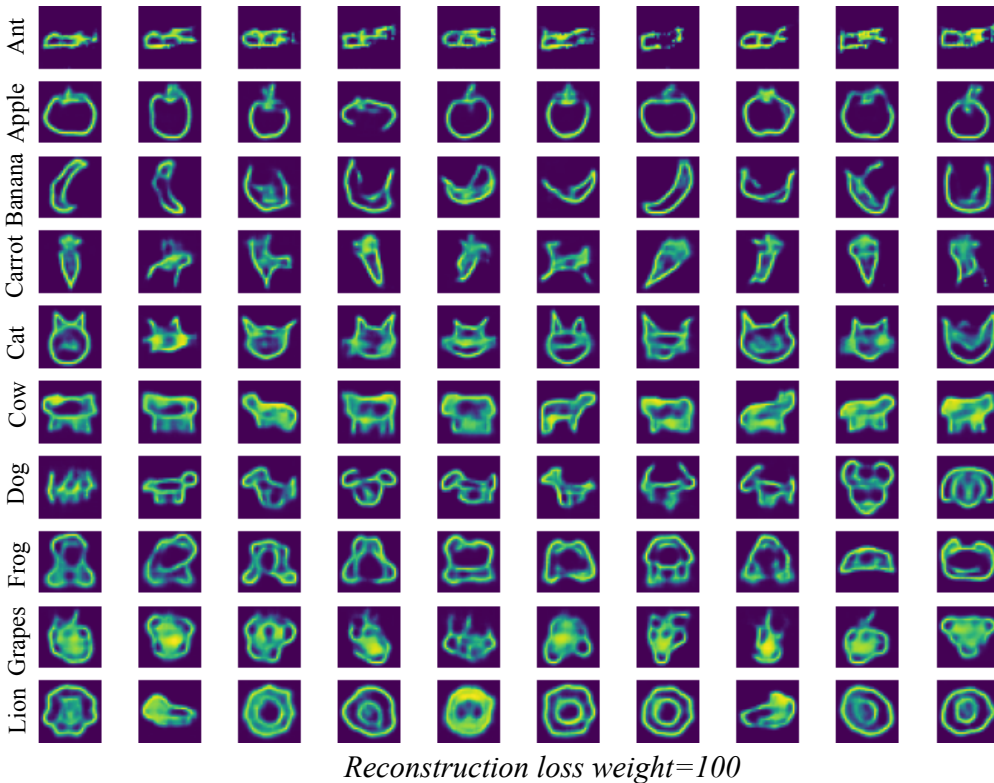
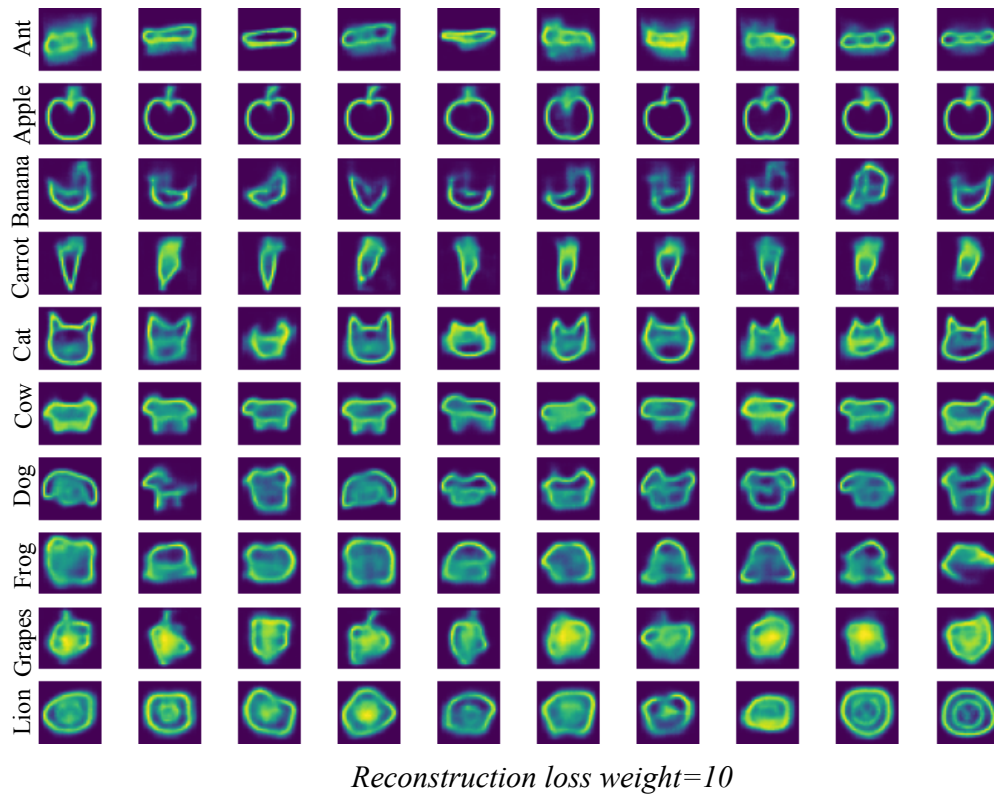
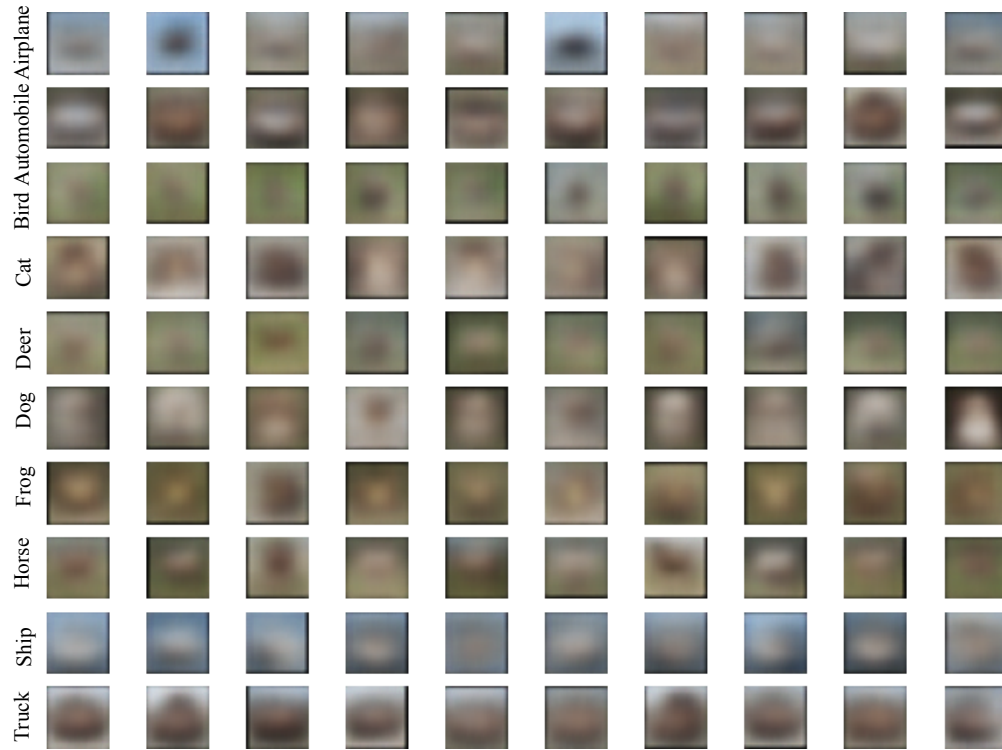
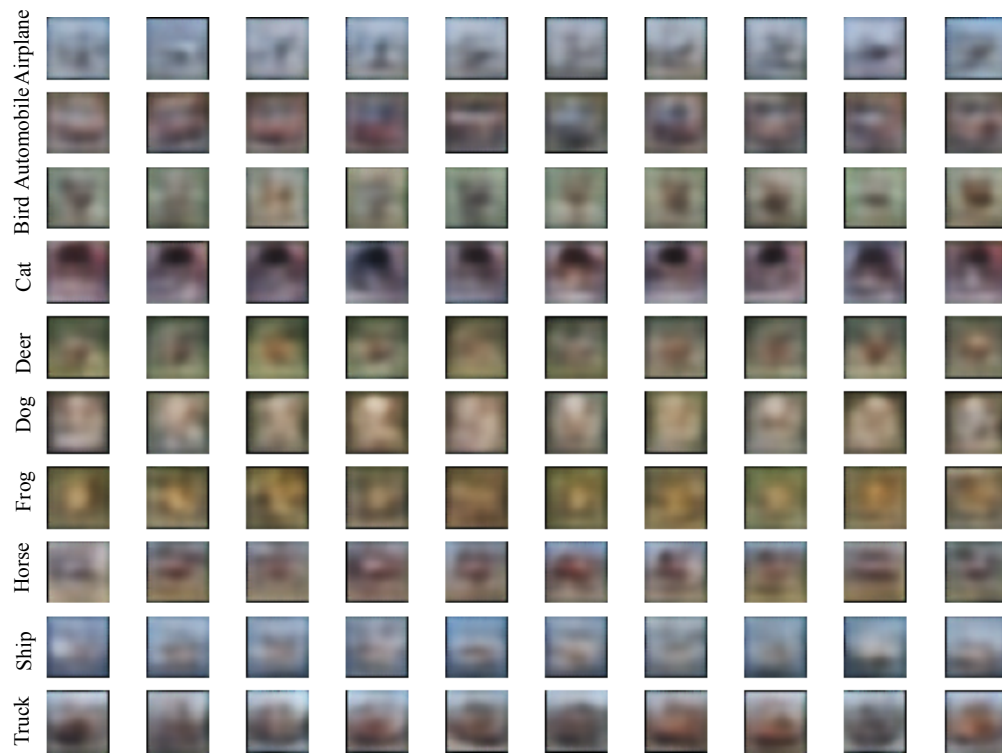


Figure 13: Prototypes for models trained on QuickDraw dataset with reconstruction loss term weighted 10 (top) and 100 (bottom). Sharper prototypes are generated with higher weight of the reconstruction loss.



Reconstruction loss weight=0.1



Reconstruction loss weight=10

Figure 14: Prototypes for models trained on CIFAR-10 dataset with reconstruction loss term weighted 0.1 (top) and 10 (bottom). Less blurry and comparatively more detailed prototypes can be observed with higher weight.

S6.10 ProtoVAE with high resolution images

To demonstrate the applicability of ProtoVAE on more complex real world datasets and high resolution images, we report here an experiment on the CelebA dataset [7]. The objective is to demonstrate the scalability, quality and diversity of the learned prototypes, and the classification task is to distinguish males and females. The images have originally a resolution of 178×218 , but are scaled to 224×224 for processing. The backbone consists of a ResNet-18 encoder followed by a decoder that resembles the architecture in Fig. 1 but is extended to 224×224 output resolution. The different sub-losses \mathcal{L}_{CE} , \mathcal{L}_{VAE} and \mathcal{L}_{orth} are weighted by 1, 1.000 and 10, respectively. The model is trained to learn 20 prototypes per class, which are depicted in Fig. 15. The test accuracy is 98.2%.

While the images have a blurry contour, several attributes clearly vary. For the women, we can distinguish different hair style, length and color, more or less open smiles, rosy cheeks and the age (second line, third and fourth from the left seem older). Interestingly, no female prototypes wear sunglasses, while the first male prototypes of the second row does. Regarding males, the face orientation seems more constant. The color of the skin and of the hair also vary. The second prototype in the first row seems bald. Despite the high accuracy, an anomaly seems to be present in form of the fourth male prototypes of the first row. The analysis of the embedding indicates that a male prototype is present within the female neighborhood. We assume that this could help to better model men with long hair, as they are not represented by other male prototypes.

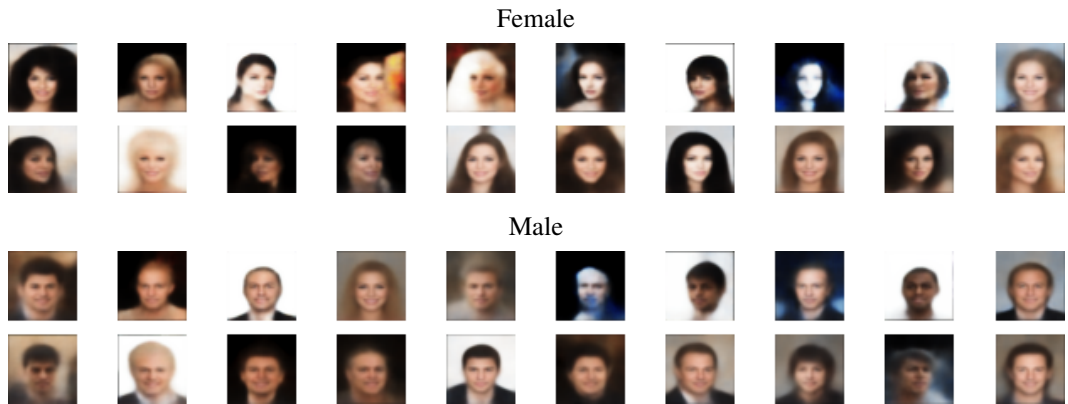


Figure 15: Prototypes learned for CelebA for ResNet-18.

S6.11 Reconstruction of test images with ProtoVAE

Since the prototype reconstructions can only be as good as the image reconstructions, we provide the test image reconstructions generated by ProtoVAE for MNIST, fMNIST, CIFAR-10, QuickDraw and SVHN in Figure 16. As can be seen, our model generates crisper reconstructions for MNIST, fMNIST, QuickDraw and SVHN as compared to CIFAR-10, which echoes the sharpness of the prototype reconstructions of Fig. 2 in the main document.

S7 Negative Societal Impacts

The proposed method will have positive societal impacts by enabling transparency while obtaining similar performance to the black-box counterparts. Nonetheless, it is still susceptible to adversarial attacks [8] similar to other existing deep learning models. A thorough inspection of the class-prototypes is thus required before it can be leveraged in safety critical scenarios to avoid spurious learning [9] or backdoor triggers [10].

References

- [1] Kaiming He, Xiangyu Zhang, Shaoqing Ren, and Jian Sun. Identity mappings in deep residual networks. In Bastian Leibe, Jiri Matas, Nicu Sebe, and Max Welling, editors, *Computer Vision – ECCV 2016*, pages 630–645, Cham, 2016. Springer International Publishing.

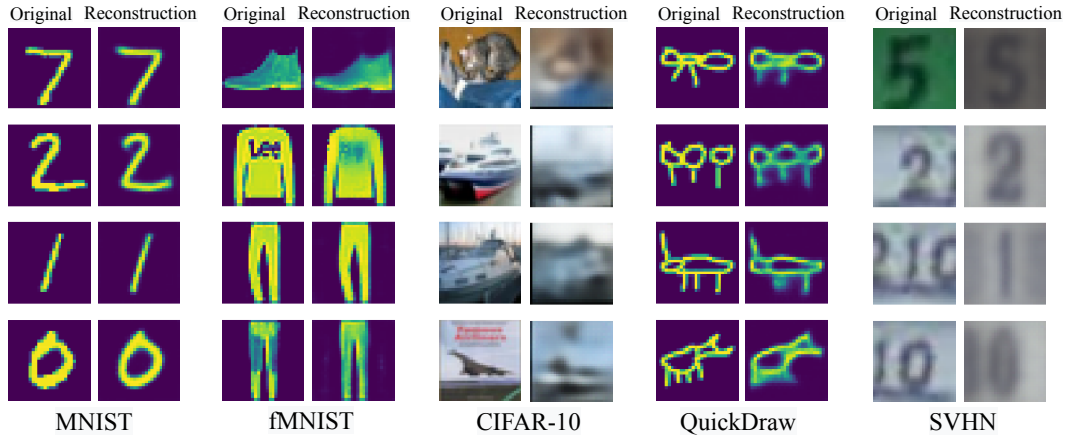


Figure 16: Visualization of test image reconstructions for MNIST, fMNIST, CIFAR-10, QuickDraw and SVHN.

- [2] Jayneel Parekh, Pavlo Mozharovskyi, and Florence d'Alché-Buc. A framework to learn with interpretation. In M. Ranzato, A. Beygelzimer, Y. Dauphin, P.S. Liang, and J. Wortman Vaughan, editors, *Advances in Neural Information Processing Systems*, volume 34, pages 24273–24285. Curran Associates, Inc., 2021.
- [3] Adam Paszke, Sam Gross, Francisco Massa, Adam Lerer, James Bradbury, Gregory Chanan, Trevor Killeen, Zeming Lin, Natalia Gimelshein, Luca Antiga, Alban Desmaison, Andreas Köpf, Edward Yang, Zach DeVito, Martin Raison, Alykhan Tejani, Sasank Chilamkurthy, Benoit Steiner, Lu Fang, Junjie Bai, and Soumith Chintala. *PyTorch: An Imperative Style, High-Performance Deep Learning Library*. Curran Associates Inc., Red Hook, NY, USA, 2019.
- [4] Chaofan Chen, Oscar Li, Daniel Tao, Alina Barnett, Cynthia Rudin, and Jonathan K Su. This looks like that: Deep learning for interpretable image recognition. In H. Wallach, H. Larochelle, A. Beygelzimer, F. d'Alché-Buc, E. Fox, and R. Garnett, editors, *Advances in Neural Information Processing Systems*, volume 32. Curran Associates, Inc., 2019.
- [5] Jia Deng, Wei Dong, Richard Socher, Li-Jia Li, Kai Li, and Li Fei-Fei. Imagenet: A large-scale hierarchical image database. In *2009 IEEE Conference on Computer Vision and Pattern Recognition*, pages 248–255, 2009.
- [6] David Alvarez Melis and Tommi Jaakkola. Towards robust interpretability with self-explaining neural networks. In S. Bengio, H. Wallach, H. Larochelle, K. Grauman, N. Cesa-Bianchi, and R. Garnett, editors, *Advances in Neural Information Processing Systems*, volume 31. Curran Associates, Inc., 2018.
- [7] Ziwei Liu, Ping Luo, Xiaogang Wang, and Xiaoou Tang. Deep learning face attributes in the wild. In *Proceedings of International Conference on Computer Vision (ICCV)*, December 2015.
- [8] Yansong Gao, Bao Gia Doan, Zhi Zhang, Siqi Ma, Jiliang Zhang, Anmin Fu, Surya Nepal, and Hyounghick Kim. Backdoor attacks and countermeasures on deep learning: A comprehensive review. *ArXiv*, abs/2007.10760, 2020.
- [9] Christopher J. Anders, Talmaj Marinc, David Neumann, Wojciech Samek, Klaus-Robert Müller, and Sebastian Lapuschkin. Analyzing imagenet with spectral relevance analysis: Towards imagenet un-hans'ed. *ArXiv*, abs/1912.11425, 2019.
- [10] Bryant Chen, Wilka Carvalho, Nathalie Baracaldo, Heiko Ludwig, Benjamin Edwards, Taesung Lee, Ian Molloy, and Biplav Srivastava. Detecting backdoor attacks on deep neural networks by activation clustering. In *SafeAI@AAAI*, 2019.